

ENHANCED ABUNDANCES IN THREE LARGE-DIAMETER MIXED-MORPHOLOGY SUPERNOVA REMNANTS

J. S. LAZENDIC¹ & P. O. SLANE

Harvard-Smithsonian Center for Astrophysics, 60 Garden street, Cambridge MA 02138

Draft version November 12, 2018

ABSTRACT

We present an X-ray study of three mixed-morphology supernova remnants (SNRs), HB 21, CTB 1 and HB 3, using archival *ASCA* and *ROSAT* data. These data are complemented by archival *Chandra X-ray Observatory* data for CTB 1 and *XMM-Newton X-ray Observatory* data for HB 3. The spectra from HB 21 and HB 3 are well-described with a single-temperature thermal plasma in ionization equilibrium, while a two-temperature thermal plasma is found in CTB 1. We found enhanced abundances in all three SNRs. The elemental abundance of Mg is clearly enhanced in CTB 1, while HB 21 has enhanced abundances of Si and S. The situation is not so clear in HB 3 — the plasma in this SNR either has significantly enhanced abundances of O, Ne and Mg, or it has marginally enhanced abundances of Mg and under-abundant Fe. We discuss the plausibility of mixed-morphology SNR models for the three SNRs and the presence of enhanced abundances. We revise a list of MM SNRs and their properties, compare the three SNRs studied here with other members of this class, and discuss the presence of enhanced elemental abundances in MM SNRs. We also report the *ASCA* detection of a compact source in the southern part of HB 3. The source spectrum is consistent with a power law with a photon index of ~ 2.7 , and an unabsorbed X-ray flux of $\sim \times 10^{-12}$ ergs cm $^{-2}$ s $^{-1}$ in the 0.5–10.0 keV band. The column density towards this source differs from that towards the SNR, and it is therefore unlikely they are related.

Subject headings: radiation mechanisms: thermal — supernova remnants — ISM: individual(HB 21 (G89.0+4.7), CTB 1 (G116.9+0.2), HB 3 (G132.7+1.3)) — X-rays: ISM

1. INTRODUCTION

Mixed-morphology (MM) or thermal composite supernova remnants (SNRs) are characterized by a shell-like morphology in the radio band and centrally peaked thermal emission in the X-ray band (Seward 1990; Jones et al. 1998; Rho & Petre 1998). Despite the relatively large number ($\sim 10\%$) of Galactic SNRs that display mixed morphology, a mechanism that is responsible for producing such a morphology has as yet not been uniquely identified. There are a few models able to produce centrally enhanced X-ray emission, such as evaporation of clouds which are left relatively intact after the passage of the SNR blast wave (e.g., White & Long 1991), thermal conduction effects in the remnant interior (e.g., Cox et al. 1999), or evolution in a medium with a density gradient viewed along the line of sight (Petrak 2001). The X-ray properties of MM remnants have been defined almost exclusively using *ROSAT* data (Rho & Petre 1998); these SNRs have: 1) centrally peaked thermal X-ray emission, with or without a fainter shell, 2) a flat radial temperature profile, and 3) X-ray emission that arises primarily from shocked interstellar material and not from ejecta. However, recent studies with *ASCA* indicate that these SNRs have a complex plasma structure, with multiple components (e.g., Rho & Borkowski 2002) and enhanced abundances (e.g., Yamauchi et al. 1999; Slane et al. 2002). We have, therefore, searched the X-ray archives for unpublished *ASCA* data on MM SNRs, in order study their spectral properties in more detail and construct a more complete picture of MM SNRs. Only three MM SNRs were found with

unpublished *ASCA* data: HB 21, CTB 1 and HB 3, all of which have low X-ray brightness emission and, consequently, low number of counts (~ 2000 in total). We also used archival *Chandra X-ray Observatory* data of CTB 1, and *XMM-Newton X-ray Observatory* data of HB 3; HB 21 has not been observed by either of the two observatories.

HB 21 (G89.0+4.7) has an angular extent of $120' \times 90'$ and a typical radio spectral index of -0.4 (e.g. Willis 1973; Reich, Zhang, & Fürst 2003). Optical emission has been detected towards the SNR, but it is not clear whether it is associated with the remnant (Willis 1973). The distance estimate of 0.8 kpc to the SNR assumes association with the molecular clouds in the Cyg OB7 complex (Humphreys 1978). CO and H I observations towards the SNR suggest an interaction with the ambient medium (Tatematsu et al. 1990; Koo et al. 2001). X-ray emission from HB 21 was first detected by the *Einstein IPC* (Leahy 1987; Seward 1990) and studied in more detail with *ROSAT All-Sky Survey* data (Leahy & Aschenbach 1996).

CTB 1 (G116.9+0.2) is a $\sim 30'$ diameter SNR with a break-out morphology in the northeast region. The radio spectral index of -0.6 (Willis 1973) and peak polarization of $\sim 40\%$ at 6 cm (Angerhofer, Kundu, & Becker 1977) confirms the nonthermal nature of the SNR. Optical emission has been detected from the SNR, with a morphology resembling that in radio (e.g., Fesen et al. 1997). The distance to the SNR is uncertain; suggested values range from 1.5 to 4 kpc (see e.g., Fesen et al. 1997). The remnant was first detected in X-rays by *ROSAT All-Sky Survey* and studied in more detail with the *ROSAT PSPC* data (Craig, Hailey, & Pisarski 1997).

¹ current address: Center for Space Research, Massachusetts Institute of Technology, Cambridge, MA 02139; jasmina@space.mit.edu

SNR HB 3 (G132.7+1.3) is $90' \times 120'$ in diameter and has radio spectral index of -0.64 (Landecker et al. 1987; Fesen et al. 1995; Reich, Zhang, & Fürst 2003). The remnant is located next to the W3 HII complex, and their association, assumed due to their proximity, implies a distance of 2.2 kpc to the SNR (Routledge et al. 1991). Diffuse and filamentary optical emission has been detected from the SNR, with the strongest emission along the western SNR shell (Fesen et al. 1995). Studies in the X-ray band have been performed using *Einstein* observations (Leahy et al. 1985; Seward 1990).

No associated radio pulsar has been found in any of the three SNRs so far (Lorimer, Lyne, & Camilo 1998). A radio pulsar PSR J0215+6218 has been discovered within (in projection) the HB 3 boundary, but it appears to be much older than the remnant and therefore not associated with the SNR (Lorimer, Lyne, & Camilo 1998). Also, an unassociated X-ray pulsar has been discovered at the edge of the north-east region of CTB 1 (Hailey & Craig 1995).

In section 2 we describe the data used in this study. In section 3 we describe results on individual remnants, and compare our results with observations at other wavelengths. In section 4 we compare our results with models for MM SNRs, and discuss the presence of enhanced abundances in MM SNRs. The conclusions are given in section 5.

2. DATA

2.1. *ASCA* data

We obtained *ASCA* data provided with the standard screening process from the HEASARC (High Energy Astrophysics Science Archive Research Center) public database. *ASCA* (Tanaka, Inoue, & Holt 1994) comprises two detector pairs: the Gas Imaging Spectrometers (GIS2 and GIS3), each with a field of view $40'$ in diameter, and the Solid-State Imaging Spectrometers (SIS0 and SIS1) with four CCDs, each of $11' \times 11'$ in size. The SIS(GIS) detectors cover an energy band between $0.4(0.6)$ and 12 keV, have spectral resolution of about $0.1(0.2)$ keV at 1 keV and combined with the X-ray telescope provide on-axis angular resolution of about $2'$ (SIS) and $3'$ (GIS).

Details of the *ASCA* observations of the three SNRs, including observational sequence numbers, date of observations, total exposure times and observing modes, are listed in Table 1. A different number of the SIS CCDs can be exposed at a time, giving 1-, 2-, or 4-CCD modes. Each SNR has been observed with at least two pointings. We used standard routines for spectral analysis of *ASCA* data in Xselect from Ftools analysis package. The data for each SNR were taken later in the mission and additional processing of the SIS data was needed to correct for degradation of the CCDs. Thus, we corrected the SIS data for charge transfer inefficiency (CTI), residual dark distribution (RDD) and dark frame error (DFE) effects (for more details see e.g., Dotani et al. 1997). However, even after these corrections, some discrepancy between GIS and SIS spectra below 1 keV can remain², potentially leading to large discrepancies between SIS- and GIS-derived column densities. Therefore, we perform a joint spectral fitting of GIS and SIS spectra for the regions common to both

² <http://heasarc.gsfc.nasa.gov/docs/asca/watchout.html>

³ <http://www.xray.mpe.mpg.de/rosat/archive/index.html>

GIS and SIS detectors, which we refer to in the text as SIS regions. We consider separately the entire portions of the remnants that are covered in each GIS detector, which we refer to in the text as GIS regions. In pointings where strong point sources were present, these were removed before extracting the spectra.

For background subtraction we used blank-sky observations from high Galactic latitude fields from which bright point-like sources were removed. Additional background X-ray emission attributed to the Galactic ridge was found to be present, mostly in the high-energy (≥ 3 keV) part of the spectrum, which was accounted for in our spectral fitting in a following manner. We subtracted a blank sky background from a spectrum created using a source-free region on the GIS detector. The residuals from this subtraction were then fitted with a model consisting of a power law; some indication of lines were present but they were too weak to be fitted by Gaussians. This was then added as a background model in spectral fits, normalized by the solid angle of the source region.

2.2. *ROSAT* data

We obtained the *ROSAT* data from the Max-Planck Institut für Extraterrestrische Physik public database³ and used them primarily to produce X-ray images of the whole remnants. The Position-Sensitive Proportional Counter (PSPC; Pfeffermann & Briel 1986) on board *ROSAT* (Trümper 1983) has field of view of $\approx 2^\circ$, spectral resolution of about 0.45 keV at 1 keV, energy range of 0.1 – 2.4 keV, and angular resolution of $15''$.

All three SNRs have extents larger than $40'$, the diameter of the central PSPC region, where the PSPC response is most uniform and sensitive. Therefore, all three sources have been observed with two or more pointings. Observational sequence numbers, dates of observation and total exposure times are listed in Table 2. For creating mosaic images from *ROSAT* PSPC data we used standard procedures in the EXSAS software package (Zimmermann et al. 1994).

We also created PSPC spectra to use in conjunction with *ASCA* data to constrain the column density (since PSPC data extend to lower energies than the *ASCA* detectors). For spectral analysis of PSPC data, standard routines in Xselect were used. Point sources were removed when creating *ROSAT* spectra. In all cases a spectrum for background subtraction was obtained from emission-free regions at the edge of the detector.

2.3. *Chandra* data

The observations of CTB 1 were obtained from the *Chandra* Data Archive. The Advanced Camera for Imaging and Spectroscopy (ACIS) on-board *Chandra* consists of two CCD arrays, the ACIS-I comprising of four CCDs arranged in a square, and ACIS-S comprising of six linearly adjacent CCDs (ACIS-S). Each CCD is about $8' \times 8'$ in size. Only six CCDs can be used at one time. ACIS covers the energy band between 0.1 and 10 keV and has an energy resolution of 0.1 keV at 1 keV, and sub-arcsecond angular resolution.

CTB 1 was observed with an ACIS exposure of 50 ks on 2002 September 14 (ObsID 2810). The observations were motivated by a search for a neutron star associated with the SNR (e.g., Kaplan et al. 2004). Four ACIS-I and two ACIS-S (S2 and S3) CCDs were used. Most of the SNR was covered with the four ACIS-I chips. Data were taken in full-frame timed-exposure mode with the standard integration time of 3.2 s. Data were reduced using standard threads in CIAO v.3.1, and calibration database CALDB v.2.28. The corrections for the effect of increased CTI and degradation of the low-energy ($E < 1$ keV) quantum efficiency of the ACIS were included in the standard procedures for CIAO v.3.1. The effective exposure time after data processing and screening for “flaring” pixels was unchanged. We used weighted response matrices for spectral fitting to account for CTI effects across the ACIS CCDs. For background subtraction we used the blank-sky observation files, following the standard procedure in CIAO v.3.1.

2.4. *XMM-Newton* data

We obtained archival *XMM-Newton* data for HB 3 from the HEASARC archive. The *XMM* European Photon Imaging Camera (EPIC) comprises three detectors: one pn and two MOS cameras. They cover the energy band between 0.2 and 12 keV, and have energy resolution of 0.15 keV at 1 keV. Their on-axis angular resolution is around 6'' FWHM and 15'' HPD, and the field of view is around 30'.

The *XMM* observation of HB 3 was carried out on 2003 February 1, with an 8 ks pn exposure and 3 ks MOS exposure (ObsID 0150960401). As for CTB 1, these observations were motivated by a search for a neutron star associated with the SNR (e.g., Kaplan et al. 2004). The EPIC-pn camera was operated in Full Frame mode with a time resolution of 73 ms, while the two EPIC-MOS cameras were operated in Full Frame mode with a time resolution of 2.6 s. The thin filter was used for all three cameras. The EPIC data reduction was performed using the SAS software package version 6.0.0. The event files used for analysis were created from observational data files (ODFs) using the SAS tasks EPCHAIN and EMCHAIN. The observations were found to be affected by periods of high particle background, and the net exposure time after filtering event files for good time intervals was 3 ks in the pn camera and 1.6 ks in each MOS camera.

In spectral analysis the blank sky observations were used for background subtraction. We used scripts supplied by the University of Birmingham *XMM* group⁴ to adjust the blank sky event file to match our data event file and to extract the source and the background regions (for more detail description of procedure see e.g., Sasaki et al. 2004). We then fitted the source spectrum and the background spectrum simultaneously, including recommended spectral components for the *XMM* detector background (see e.g., Lumb et al. 2002).

2.5. *Radio*

For a comparison with radio data we used the 92 cm observations from the Westerbork Northern Sky Survey (WENSS), obtained from the SkyView public database.

⁴ <http://www.sr.bham.ac.uk/xmm2/>

We smoothed the radio data from their original resolution of $54'' \times 54'' \text{ cosec}(\delta)$ to $2'-3'$ in order to improve signal-to-noise in the images.

3. RESULTS

To examine the SNR morphology we used both PSPC and GIS images. We generated exposure-corrected PSPC images using photons with energies between 0.2 and 2 keV. The GIS images were exposure-corrected, background subtracted and masked in regions where the exposure falls below 15% of the maximum value. Photons with energies between 0.7 and 10.0 keV were used for making the GIS images.

The final spectral analysis was performed using the *ASCA* data alone, because adding the *ROSAT* PSPC spectra did not improve the fit or constrain the parameters derived from spectral fitting significantly. We used a model for interstellar absorption by Morrison & McCammon (1983), in combination with a model for an optically thin thermal plasma in collisional ionization equilibrium (CIE; VRAY(MOND); Raymond & Smith 1977). We also used a plane-parallel time-dependent ionizing plasma model (VPSHOCK; Borkowski, Lyerly, & Reynolds 2001), and an ionizing collisional plasma model which assumes a single ionization parameter (VNEI; Mazzotta et al. 1998). The VPSHOCK model can provide useful information on emission from the SNR boundary regions (e.g., NE region in CTB 1 or N3 region in HB 3) where we can expect a range of ionization timescales if the evolving shock (i.e. forward shock) is present. The central SNR regions were presumably shocked some time ago, and equilibrium models such as VRAY or VNEI are more appropriate. The GIS data can suffer from gain variations, and we applied gain corrections when fitting GIS data resulting in gain adjustments of 1%–3%; these corrections did not always improve the fit, nor did they change the fit parameters significantly and are, therefore, not used in the final fits. All the spectra were grouped to ensure a minimum of 25 counts per bin. Due to the low X-ray surface brightness of the SNRs, a detailed spatially resolved spectral analysis for each pointing was not possible. However, since *ASCA* pointings cover different regions of the SNRs, they do provide spatially resolved spectral analysis to a limited extent.

3.1. HB 21 (G89.0+4.7)

3.1.1. *Morphology*

Figure 1 shows the *ROSAT* PSPC mosaic image of HB 21, composed from six pointings and smoothed with a Gaussian of 5'' FWHM. Regions covered by the *ASCA* detectors are also marked. As shown before (Leahy & Aschenbach 1996), the X-ray emission is centrally concentrated, and appears elongated in the northwest-southeast direction. The *ASCA* GIS image of the central part of the SNR, and the overlay of the GIS contours onto the *ROSAT* image are shown in Figure 2. There is a good correlation between the two images. The X-ray emission from the SNR appears clumpy both in the PSPC and GIS images. The GIS image appears to have a half-circular

shell-like feature oriented northeast-southwest and stretching through the center which is not obvious in the PSPC image. We note that this shell coincides with the edge of one of the GIS (P1) pointings, and thus could be an artifact of the mosaicing. To investigate this structure in more detail, we produced an exposure-corrected image of pointing P2 alone. The half-circular feature is still present, which suggests it is real. The two brightest clumps of X-ray emission are located along this bright shell in the GIS image and they do not have corresponding bright emission in the PSPC image. This suggests that the bright shell and the two bright clumps, have the harder spectrum than the other parts of the SNR that have corresponding PSPC emission. We also produced soft (0.7–2.5 keV) and hard (2.5–10.0 keV) band GIS images, but we found no significant differences, probably due to the relatively low number of counts available.

Radio and X-ray emission from HB 21 are compared in Figure 3, which shows that there is no radio emission corresponding to the central X-ray emission. The fainter, diffuse X-ray emission extends towards the radio limbs in all directions except for the east. Leahy & Aschenbach (1996) suggested that the emission from the eastern SNR shell is affected by absorption from the molecular clouds associated with HB 21, which have column densities of $(2.5\text{--}5.5)\times10^{21}$ cm $^{-2}$ (Tatematsu et al. 1990). Optical images also imply that extinction towards the eastern SNR region is higher than elsewhere (Willis 1973). Tatematsu et al. (1990) suggested an interaction between the H I and CO gas along the eastern SNR shell, on the basis of morphology. Observations with improved spatial resolution by Koo et al. (2001) confirmed the presence of molecular gas along the eastern SNR boundary, but found little correlation between features in the molecular cloud and the SNR brightness distribution, or small-scale morphology. They also found no direct kinematic evidence of interaction (e.g., broad molecular lines) between the eastern clouds and the SNR shell. Instead, broad molecular lines are found toward the bright radio regions in the north and south part of the SNR shell. The IR emission is present along the SNR boundary, and shows large-scale correlation with CO emission. Using the 60 and 100 μ m ratio, Koo et al. (2001) found additional support that interaction at the eastern SNR shell is unlikely, while the IR emission from the north and south clouds has a higher 60/100 μ m ratio, suggestive of shock origin. The northern and southern bright radio regions lack X-ray emission, as shown in Figure 3, indicating that X-ray emission from the SNR has been absorbed or the shock could have gone radiative due to interaction with molecular clouds.

3.1.2. Spectra

The joint fits to the GIS and SIS spectra from the two SIS regions of HB 21 are shown in Figure 4. The He-like Si line feature is prominent in both the GIS and SIS data. The VRAY model gave a satisfactory fit to the spectra, but the VNEI model gave an improved fit (4σ significance) in most cases; the VNEI fit parameters are summarized in Table 3. We note that high values of $n_e t$ imply that plasma is close to, or have reached equilibrium, and thus, VRAY model is acceptable as well. The fit with solar abundances was improved significantly for some regions when the Si

and S abundance was thawed. There is no significant variation in temperature between the two pointings, but there could be some variation in the column density, with the P2 pointing having higher column density than the P1 pointing. Slightly enhanced abundances imply that the X-ray plasma in HB 21 comprises supernova ejecta mixed in with the swept up shocked material. The bright shell-like feature revealed in the GIS image could be then formed by the reverse shock.

Spectral parameters obtained from the *ASCA* data are broadly in agreement with the fit parameters derived from the previous study using *ROSAT* data alone (Leahy & Aschenbach 1996). In general, column densities inferred from *ASCA* spectra tend to be higher than those from the PSPC. This is a direct result of the different band-passes. The column density of $\approx 4\times10^{21}$ cm $^{-2}$ derived here seems high for an SNR as close as 0.8 kpc, but this column density is comparable to the column density of the eastern molecular clouds observed by Tatematsu et al. (1990). Thus, it seems that most of the column density to the SNR is coming from the eastern molecular cloud, and it is plausible that the eastern SNR shell could be more absorbed than the rest of the SNR. Another possibility is that the shock has encountered a nearly circular (in projection) cavity edge in the southern half of the remnant (as in the Cygnus Loop SNR).

3.2. CTB 1 (G116.9+0.2)

3.2.1. Morphology

In Figure 5 we show the *ROSAT* PSPC image created from the two CTB 1 pointings, as well as regions covered by the *ASCA* and *Chandra* observations. The X-ray emission extends from north-east to south-west with the brighter emission to the south-west, as shown by Craig, Hailey, & Pisarski (1997). The GIS image and its comparison to the PSPC image is shown in Figure 6. There are several point sources in the field, one of which is an unrelated X-ray pulsar (undetected in radio band) in the north-east region outside the SNR radio shell. The two point sources prominent in the center of the SNR are also obvious in the GIS data. There is a good overall correlation between the diffuse SNR emission in the GIS and PSPC images. As for HB 21, we produced soft and hard band *ASCA* images to investigate possible spectral variations, but found no significant differences.

Comparison with the 92 cm WENSS radio image in Figure 7 shows that X-ray emission is concentrated inside the radio shell, and has a break-out morphology in the north-east, extending further than the radio emission. CTB 1 has almost perfect spherical radio morphology which suggests that the blast wave has been expanding into a relatively uniform ambient medium, except for in the north-east. The optical emission resembles the radio emission, showing limb-brightened filaments and diffuse emission in the remnant's interior (e.g., Fesen et al. 1997). The north-east region has been suggested to be a blow-out of the SNR shock into a lower-density medium, or an unrelated SNR associated with the X-ray pulsar (Hailey & Craig 1995). The morphology of optical filaments corresponding to the north-west X-ray emission supports the blow-out scenario (Fesen et al. 1997). H I gas in the region is distributed mostly in the southern half of the remnant, having an arc-

like appearance (Landecker, Roger, & Dewdney 1982; Yar-Uyaniker et al. 2004), and suggests that the remnant has been influenced by the density distribution of the ambient gas.

3.2.2. Spectra

The spectra from the GIS regions in the W and NE pointings are shown in Figure 8. Bright point sources have been excluded when extracting the source spectra. No line features are prominent in the GIS spectra; the spectra are fitted well with a single-component VRAY model with solar abundances. The VPSHOCK model gives fit parameters for the NE region consistent with those from VRAY model. The SIS and GIS spectra from the SIS-covered W pointing are also shown in Figure 8; some indication of a Mg line is present. A single-component VRAY model to these spectra resulted in large residuals ($\chi^2 \approx 2$), and addition of a second thermal component improved the fit significantly. The two-component model requires a cold plasma component with $kT \sim 0.2$ keV, and a warm plasma component with $kT \sim 0.8$ keV. The spectra from the SIS regions prefer enhanced abundances of Mg, but only in the higher temperature component. The same hard component can be added to the GIS spectra, but does not improve the fit significantly (the improvement is less than 2σ) and it is about 100 times weaker than the soft component. This implies that the hard component is more diluted in the larger area covered by the GIS field of view, and is, therefore, concentrated more in the center of the SNR. The fit parameters are summarized in Table 4. The column density and temperature of the cooler plasma component we derive here are consistent with those derived from the previous study with the *ROSAT* data alone Craig, Hailey, & Pisarski (1997).

A *Chandra* spectrum has been obtained from four 5'-square regions from four ACIS-I chips, covering the brightest part of the SNR. As mentioned before, blank-sky observations were used for background subtraction. We have verified that there is no significant contribution from the Galactic ridge emission by comparing the blank sky spectrum with that of the local background taken from the source-free region. The ACIS spectra are shown in Figure 8 and the spectral fit parameters are listed in Table 4. As for W-SIS regions from the *ASCA* data, the ACIS spectra require a two-component thermal model, but prefer a nonequilibrium VNEI model ($\chi^2 = 374.4$ for 468 d.o.f.) model to VRAY ($\chi^2 = 433.6$ for 470 d.o.f.). The spectral parameters obtained with *Chandra* are consistent with those obtained with SIS-covered *ASCA* spectra, including the detection of enhanced abundances of Mg. Lines of O and Ne+Fe-L blend are also clearly visible in the ACIS spectra. As in the case of HB 21, detection of enhanced abundances in CTB 1 implies the presence of ejecta in this SNR.

There are several point sources from the WGA *ROSAT* Point Source catalogue (White, Giommi, & Angelini 2000) towards CTB 1. One of the sources is the unrelated X-ray pulsar RXJ 0002+6246 (1WGA J0002.9+6246 Hailey & Craig 1995) located outside the SNR shell in the north-eastern region. We detected 120 ± 40 background-subtracted counts within the 6'-radius circle at the location of the X-ray pulsar, but no compact source is obvious

in the GIS data. Other WGA sources also have a low number of counts, and we are unable to investigate their nature in more detail.

3.3. HB 3 (G132.7+1.3)

3.3.1. Morphology

The *ROSAT* PSPC image, composed of four pointings towards HB 3, is shown in Figure 9, including the SNR regions covered by the *ASCA* and *XMM* detectors. The PSPC image has been smoothed with a Gaussian of 5" FWHM. The X-ray emission is brightest in the center, with fainter emission extending to the north and south. As noted by Leahy et al. (1985), the central emission appears as a ring with a radius of $\sim 16'$. The GIS image and its overlay with the *ROSAT* image are shown in Figure 10. The GIS image also shows bright emission corresponding to the PSPC ring. The X-ray emission from the north region shows good correlation between GIS and PSPC data, and there is a prominent bright clump between the central and north pointing. As for HB 21 and CTB 1, we produced soft and hard band *ASCA* images to investigate possible spectral variations, but we found no significant differences. In the south region, however, the *ASCA* observations reveal the presence of a compact source, possibly coinciding with the *ROSAT* All Sky Survey source 1RXS J021703.6+620136 (within the position error of 14"). We analyze this source in more detail in section §3.3.3.

The comparison between the radio and X-ray emission is shown in Figure 11. As mentioned before, HB 3 is located close to the W3 H II region, which can be partially seen in the south-east corner of the radio image in Figure 11. There is not much correlation between the radio and X-ray morphologies, as noted before by Leahy et al. (1985). Diffuse X-ray emission extends to the north radio shell, and weaker diffuse emission extends to the southern radio limb. It is not clear whether this southern emission belongs to the SNR, or to a newly detected compact *ASCA* source. Routledge et al. (1991) suggested that the fainter diffuse emission at the SNR's north part is caused by a density gradient produced by evolution in a cavity, rather than by a Galactic plane gradient, because the elongation of the SNR is not perpendicular to the Galactic plane ($\sim 75^\circ$). The bright inner SNR ring was suggested to be due to a second SNR, a pre-supernova circumstellar shell, or an unusual density distribution in the ejecta (Leahy et al. 1985). The lack of X-ray emission in the south-eastern region was attributed to absorption along the line of sight to the remnant (Leahy et al. 1985), which was supported by the detection of a CO cloud (Huang & Thaddeus 1986), suggested to be interacting with the remnant on the basis of morphological agreement (Routledge et al. 1991). OH(1720 MHz) masers, which are recognised as the signpost for molecular cloud interaction with an SNR (e.g., Wardle & Yusef-Zadeh 2002), have been detected towards the W3/HB 3 complex. One of the masers is located very close to the SNR, with a velocity close to the systematic velocity of the gas associated with the remnant; the maser is, however, located outside the SNR shell and is believed to be associated with star-forming phenomena rather than the SNR shock (Koralesky et al. 1998). Optical emission from the SNR was found to be well-correlated with the ra-

dio emission, with a multiple shock structure found in the western SNR shell and lack of emission in the southeast region (Fesen et al. 1995).

3.3.2. Spectra

The GIS and SIS spectra from the two SIS regions (SIS0 and SIS1 cover different regions; see Fig. 9) in the central pointing towards HB 3 are shown in Figure 12. Bright point sources have been excluded when extracting the source spectra. The VRAY model with enhanced Mg abundances was able to give a satisfactory fit to the spectra from the central SIS0 pointing, but the region corresponding to the SIS1 pointing does not require enhanced abundances. For completeness, we list the Mg abundances for both SIS pointings in Table 5, together with other fit parameters. The joint fit to the GIS and SIS spectra from the north pointing was performed for the two SIS CCDs separately (marked N3-south and N3-north in Fig. 9). We also applied the VPSHOCK and VNEI models to the N3 regions, and the spectral parameters were consistent with those from the VRAY model. The spectral fits to the N3-north region give solar abundance and higher plasma temperature than the central SNR region. That is also the case for the N3-south region, with a difference that the column density is slightly lower than in the central region. If we freeze N_{H} to the value from the N2 regions when fitting the N3 regions, we get a plasma temperature consistent with the N2 pointings for N3-north, while N3-south still requires a slightly higher temperature. Leahy et al. (1985) reported that the plasma temperature decreases from 1 keV in the center, to 0.3 keV towards the edge. We find a low temperature in the SNR center with the *ASCA* data and that the plasma temperature, and possible the column density, varies non-uniformly from the center of the remnant to the north.

An *XMM* spectrum obtained from the 5'-radius region from the central region of the EPIC-pn detector is shown in Figure 13. No spectra were obtained from the EPIC-MOS detectors due to a very low number of counts in these two detectors. Because the diffuse emission from the remnant covers the whole detector, we used the blank sky observations for background subtraction. The source and background spectrum were fitted simultaneously. The background was modeled with two thermal components using the VRAY model with temperatures 0.08 and 0.2 keV (Lumb et al. 2002), in combination with a power law model and zero-width Gaussians to account for the detector background. The SNR emission was modeled with the VRAY or VNEI model, which was not applied to the background spectrum. We achieved a good fit with a single-temperature plasma component with enhanced Mg abundance ($\chi_{\nu}^2=1.21$), and the fit parameters are consistent with those from the central *ASCA* (N2) pointing. However, some residuals were still present in the *XMM* spectrum in the 0.6–1.0 keV range. This is the energy range where O and Ne lines are present, as well as Fe L-shell lines (e.g., Masai 1997; Brickhouse et al. 2000). Therefore, we thawed the O elemental abundance next, in addition to Mg, which improves the fit significantly. We list parameters of this fit in Table 5. However, if the Ne abundance is thawed next, the fit is also improved significantly, but the column density and temperature change considerably

($N_{\text{H}} \sim 0.5 \text{ cm}^{-2}$ and $kT \sim 0.3 \text{ keV}$) and the fit values are not consistent with *ASCA* results anymore. Thawing Fe abundances no longer improves the fit. On the other hand, if Fe is thawed first, in addition to Mg alone, the fit is also improved and results in slightly enhanced Mg and under-abundant Fe. However, the column density and temperature also change to above values. Therefore, we can not determine with certainty the elemental abundances of Ne and Fe, as well as the N_{H} and kT values sampled by the *XMM* region. These issues will possibly be resolved with new data obtained recently with *XMM* towards four regions of HB 3, including the central region.

In summary, the *ASCA* data for HB 3 indicate that there is an enhanced abundance of Mg present only in the center of the remnant. The *XMM* data suggest a few possibilities, including enhanced abundances of Mg, Ne and O, or enhanced abundances of Mg and sub-solar abundances of Fe. It is not too surprising to have different fit parameters from the *XMM* and *ASCA* spectra, because *XMM* is more sensitive than *ASCA* at lower energies, and the regions sampled by the two observatories differ somewhat. As for the origin of the inner ring in HB 3, our data are not sensitive enough to discriminate between the scenarios suggested above.

3.3.3. Point sources in HB 3 field

There are a few point sources identified from the WGA catalogue present in the field towards HB 3, but none of them have enough counts in the *ASCA* data to be analyzed here. No X-ray emission was detected from the radio pulsar PSR J021800.0+621000, which is not surprising considering its age ($\sim 10^6$ yr; Lorimer, Lyne, & Camilo 1998).

To investigate the nature of the bright southern source detected with *ASCA* we used only the SIS spectra, shown in Figure 14, because the SIS detectors have a smaller point spread function than the GIS detectors. The source spectra were extracted from the 4' circular region around the compact source, resulting in about 200 background subtracted counts, and the background spectra are extracted from the thin ring-like region around the source region. While a thermal model of plasma in equilibrium (RAY), and also a bremsstrahlung model can be rejected because of statistically unacceptable fits ($\chi_{\nu}^2 \sim 3$), both a power law and blackbody models give reasonably good fits to the source spectra. The fit parameters for the power law model are: a column density of $N_{\text{H}}=2.9 (1.8-4.1) \times 10^{21} \text{ cm}^{-2}$, photon index of $\Gamma=2.74 (2.39-3.16)$, and $\chi_{\nu}^2 = 1.60$ for 27 degrees of freedom. The fit parameters for the blackbody model are: $N_{\text{H}}=1.1 (0.4-2.1) \times 10^{21} \text{ cm}^{-2}$, temperature of $kT=1.91 (1.35-2.75) \text{ keV}$, and $\chi_{\nu}^2 = 1.90$ for 27 degrees of freedom. An unabsorbed X-ray flux in the 0.5–10.0 keV band is, for both models, $10^{-12} \text{ ergs cm}^{-2} \text{ s}^{-1}$. The column density appears to be, for both cases, lower than from the SNR, suggesting that the source is probably not at the same distance as the SNR.

The photon index from the compact source is softer than that of classical young pulsars which are found with photon index values between 1.1–1.7; it is also harder than the photon index values found in compact central objects (CCOs) and anomalous X-ray pulsars (AXPs) with a pho-

ton index of ~ 4 (e.g. Chakrabarty et al. 2001). There is a small-diameter source present in the WENSS radio image that coincides with the location of the *ASCA* source. Landecker et al. (1987) derived a steep radio spectral index of -0.98 ± 0.8 , using observations at 408 MHz and other available frequencies. The field towards this region is crowded with optical and infrared source, but since we do not know the exact position of the possible point source, we cannot determine if there is an optical or infrared counterpart to the *ASCA* source. Further observations are needed to establish the exact nature of this source.

4. DISCUSSION

4.1. SNR properties

Our study confirms the thermal nature of the central X-ray emission in three SNRs — HB 21, CTB 1 and HB 3 — classified as mixed-morphology SNRs. In addition, we detected enhanced abundances in all three SNRs.

HB 21 shows a flat temperature of around 0.6 keV across its center, which is similar to value often found in MM SNRs (Rho & Petre 1998). Unlike for the other two SNRs studied here, there are no *ASCA* pointings towards the edge of the SNR shell in HB 21, and therefore, we do not have a complete knowledge of the temperature distribution in this remnant. *ASCA* data show a possible column density variation in HB 21, with higher column density in the P2 pointing. This is consistent with a suggested interaction with molecular clouds in that region. There are bright radio indentations north and south from the P2 pointings and this is where Koo et al. (2001) detected broad molecular lines. Interactions with dense material may have resulted in the formation of a radiative shock in these regions, which would explain why there is no X-ray emission corresponding to these bright radio regions, while there is X-ray emission corresponding to the radio shell extending to the west, right next to it. The spectrum of HB 21 is dominated by the Si line, and we found enhanced abundances of Si and S in the center of the SNR.

Observations of CTB 1 reveal two plasma components in this remnant, one around 0.2 keV with solar abundances, and the other around 0.8 keV with enhanced Mg. Line features between 0.6 and 1.5 keV are visible in the *Chandra* spectrum of CTB 1. We found enhanced abundances of Mg for the higher temperature component only from SIS and ACIS regions in CTB 1, implying the presence of ejecta in the center of CTB 1. The presence of two thermal components is similar to what is seen in *ASCA* observations of IC 443 (Kawasaki et al. 2002), although without enhanced abundances. The higher sensitivity of the IC 443 data allowed spatial identification of its spectral component as a cool X-ray shell and warmer central region. Indeed, IC 443 and CTB 1 share similar morphology, both having a blow-out region on one side and interaction with dense H I material on the other side. The 0.2-keV component in CTB 1 could thus originate from a cooled SNR shell, since we see X-ray emission in CTB 1 extending up to the radio shell, mostly in the north-west side. H I material is densest in the south-east region and the radio continuum is brightest here (Landecker, Roger, & Dewdney 1982), so it could be that the SNR shock cooled down significantly here due to an encounter with the denser material. On the other hand, the plasma in CTB 1 might be similar to that in

W28, where two distinct plasma components are found in the center of the SNR, although without enhanced abundances; the soft plasma component here was suggested to originate from denser clumps embedded in diffuse hot gas (Rho et al. 2004).

For HB 3 the situation is not so clear. *ASCA* observations indicate a small but significant column density and plasma temperature variation from the center of the SNR towards the northern shell. There seems to be a single plasma component present, with enhanced elemental abundances of Mg in the center of the SNR. However *XMM* data allow for a different possibility, which results in a lower column density in the center and a higher plasma temperature than derived from the *ASCA* data, as well as additional enhanced abundances of O and Ne or sub-solar abundances of Fe.

4.2. MM models

A characteristic feature of MM SNRs is a flat temperature profile. Due to the low number of counts in the SNRs studied here, we are unable to derive the radial temperature distributions. Nevertheless, we consider different models that can produce centrally-concentrated X-ray emission in the three SNRs studied here.

4.2.1. Evaporating clouds

One of the earliest MM SNR models invokes evaporation of clouds which are left relatively intact after the passage of the SNR blast wave (e.g., White & Long 1991). In such a case most of the X-ray emitting gas is due to dense embedded molecular material that evaporates in the SNR interior due to saturated thermal conduction in the hot gas. This model depends on the C/τ ratio, where C is the ratio of the mass in the clumps to the mass of inter-cloud medium, and τ is the ratio of the cloud evaporation time to the SNR's age. Ratio $C/\tau = 3-5$ is found to be the most appropriate for the steep radial surface brightness profiles of MM SNRs (White & Long 1991). The remnant is assumed to still be in the adiabatic phase, and the post-shock temperature is thus related to the observed temperature of the X-ray gas in the Sedov phase, scaled by a K/q factor which depends on the C/τ ratio (White & Long 1991):

$$T_s = T_{\text{Sedov}} \times (K/q) = 0.78 kT_x (K/q). \quad (1)$$

Typical K/q values for $C/\tau=3-5$ are 1.0–1.3. Note that T_s refers to the case where electron-ion equilibrium is assumed. The Rankin-Hugoniot relation for the temperature of shocked gas with adiabatic index $\gamma = 5/3$ is used to derive the velocity of the blast wave:

$$v_s = \left(\frac{16kT_s}{3\mu m_H} \right)^{1/2}, \quad (2)$$

where $\mu = 0.604$ is the mean atomic weight, and the age of the remnant is:

$$t = 2r_s/5v_s. \quad (3)$$

The explosion energy is found from

$$E = \frac{E_{\text{Sedov}}}{(\gamma + 1)K} = \frac{16\pi(1.4n_0m_H)}{25(\gamma + 1)K} \frac{r_s^5}{t^2}. \quad (4)$$

The SNR dynamical parameters for the central SNR pointings obtained from this model are listed in Table 6. Although significant evidence exists that CTB 1 and HB 3

are in the radiative phase of evolution and, thus, the evaporating model is unlikely scenario for them, we list parameters of this model for all the SNRs for completeness. The SNR parameters used for calculations, like shock radius R , emission volume V , distances d to the SNRs are also listed in Table 6. The post-shock electron densities n_{H} are derived from X-ray emission measure $EM = n_{\text{H}}^2 fV/4\pi d^2$. The emission volume V was taken to be a slab whose area corresponds to the spectral extraction region, and for depth we took half of SNR diameter, the later being a simple way to account for the fact that X-ray emission does not fill the whole remnant. For comparison, we also list the values obtained using Sedov solutions in Table 6. The observed densities for Sedov solution range from low values between $\sim 0.07 \text{ cm}^{-3}$ in HB 3 to more typical values of $\sim 0.4 \text{ cm}^{-3}$ in CTB 1. We note that these values may not represent the immediate post-shock densities for the Sedov solution, but we carry out the calculations to illustrate how SNR parameters change depending on the SNR model applied. The SNR age ranges from 5×10^3 years in HB 21 to 3×10^4 years in HB 3. The explosion energy derived from Sedov solutions is more than one order of magnitude lower from the canonical explosion energy of 10^{51} ergs. The explosion energy derived from the evaporating cloud model is higher than for the Sedov model, but still an order of magnitude lower than 10^{51} ergs in most cases. This is often the case when evaporation model is applied to MM SNRs (e.g., Harrus et al. 1997; Slane et al. 2002).

4.2.2. Radiative SNRs

Another model has been applied to explain the emission for the mixed morphology SNR W44 (Cox et al. 1999; Shelton et al. 1999) as due to the effect of thermal conduction in the interior of the radiative remnant that is expanding into a density gradient. In the radiative phase of SNR evolution the shock temperature falls below $\sim 0.1 \text{ keV}$, and there is no X-ray emission above $\sim 1 \text{ keV}$ from the SNR shell. The soft X-ray emission from the radiative shock is readily absorbed, and so the central hot region of the SNR dominates the X-ray emission. The Sedov model for this phase gives a high temperature but low density in the center of the remnant which would result in low emission from the center. Thermal conduction via Coulomb collisions between the electrons and ions inside the hot plasma (Spitzer 1956) can reduce the central temperature and increase the central density, which can dramatically increase the brightness of the central emission. Thermal conduction was thought not to be significant in SNRs because of the presence of strong magnetic fields, but it is possible that the magnetic fields get swept up from the SNR interior which enables efficient thermal conduction.

We examine the possibility that the three SNRs studied here are in the radiative phase. All three SNRs are found with dense gas present in their vicinity, as suggested by H I and CO observations. The radiative shell size R_s and shell formation time t_{shell} for an SNR can be found from (Cox et al. 1999):

$$R_s \approx 12E_{51}^{1/8} t_{\text{sh},20}^{3/4} \text{ pc}, \quad (5)$$

$$t_{\text{shell}} = 53 \times 10^3 E_{51}^{3/14} n_{\text{sh}}^{-4/7} \text{ yr}, \quad (6)$$

where n_{sh} is the ambient gas density and $t_{\text{sh},20} = t_{\text{shell}}/(20000 \text{ yr})$.

Using a canonical SNR explosion energy $E_{51} = 10^{51}$ ergs, we plot R_s and n_{sh} for a range of t_{shell} values in Figure 15. Taking the observed shock radius for each remnant (as found from radio observations) to be the radius at which the SNR has entered the radiative phase we can set a lower limit to the ambient density. The resulting time required for the onset of the radiative phase at the current SNR radius (which is an upper limit to the age, assuming the radiative phase was reached sometime before the current epoch) is about two times higher than the age derived from the Sedov and evaporation cloud models for all three SNRs. Note that uncertainties in the radius lead to uncertainties in the derived density and shell formation time, but these are not significant. If thermal conduction is important in the SNR interior, then the radiative shell formation stage could be reached even earlier. More detailed modeling is required to determine whether thermal conduction effects are fully consistent with the observations.

To estimate the central density n_c of the X-ray emitting gas we use relations from Cox et al. (1999):

$$n_c/n_{\text{sh}} = 0.334(t_{\text{cool}}/t)^{18/25}[(t/t_{\text{cool}})^{1/25} - 0.44^{1/25}]^{18/71} \quad (7)$$

where $t_{\text{cool}} \approx (7/6)t_{\text{shell}}$ is the cooling time for the SNR. The calculated n_c values are also plotted in Figure 15; these represent lower limits for each indicated SNR. They are significantly higher than the electron densities derived from the emission measure in Table 6 for HB 21 and CTB 1, but comparable for HB 3. We note that equation 7 corresponds to full conduction, but it is weakly dependent on this; reduction of the conduction by a factor of ten reduces the central density by a factor of less than two. Thus, even though the full conduction case is inconsistent with the assumptions made in deriving the onset of the radiative phase (because the internal pressure is reduced in the presence of conduction), the associated central density predictions are not particularly sensitive to this. We conclude that the ambient densities required for the SNRs discussed here to reach the radiative phase by the current epoch are consistent with inferred densities around the remnants, but that the central densities derived by our spectral fits are lower than expected under such a scenario. It is possible that the assumed volume for the X-ray emission region has been overestimated in deriving these densities, but current data are too sparse to better quantify the distribution of the multiple emission components. Deeper X-ray observations of these SNRs are needed to more fully investigate their evolutionary states.

4.3. Presence of ejecta in MM SNRs

The detection of the enhanced abundances in three MM SNRs studied here suggests that we detect contributions from shocked SN ejecta. Enhanced abundances have been found in a significant number of MM SNRs now. In Table 7 we list the SNRs identified as MM type, and briefly summarize their properties. Of 23 SNRs, 10 show evidence for enhanced abundances, and 5 of those detections are confirmed by *Chandra* or *XMM* observations, including two SNRs studied here. Some of the remnants have multiple-component plasmas and enhanced abundances,

like CTB 1, possibly indicating that the ejecta and swept-up components are spectrally resolved. In other SNRs with a single component plasma and enhanced abundances, like HB 21 and HB 3, the ejecta component might be more mixed with swept-up material and better statistics are needed to resolve the two components. We excluded W49B from the sample of MM SNRs with enhanced abundances because this remnant might be ejecta-dominated rather than swept-up mass dominated, and therefore not a true MM SNR (for a different view see Kawasaki et al. 2005). However, W49B might prove to be in a pre-MM stage, while 3C 391, which has solar abundances, might represent a later stage of MM SNRs when ejecta is well mixed with swept-up mass. Kes 79 is another SNR classified as MM that has solar abundances (Sun et al. 2004). However, Kes 79 has a unique multiple-shell structure rather than diffuse or clumpy central brightness like other MM SNRs, and therefore might also not be a true MM SNR (Sun et al. 2004). We also note that W28 presently exhibits different properties from all of the other MM SNRs. W28 has a cool shell in the north-west region where the SNR is encountering a dense molecular cloud, and a hot plasma in the south-west region where the SNR seems to be breaking out in a lower density region (Rho & Borkowski 2002). These two components have radio counterparts, and are obviously related to the large-scale inhomogeneities in the ambient medium that are influencing the radio emission as well. However, it is the two-temperature thermal central emission of W28 that is most intriguing. Preliminary *Chandra* results imply that soft emission is coming from a clumps embedded in hot diffuse gas (Rho et al. 2004).

It is often found that the evaporating cloud or thermal conduction models are able to explain individual MM cases, but there is general failure to accurately reproduce the central brightness profile, and a contribution from SN ejecta was suggested to play role in enhancing central brightness (e.g., Slane et al. 2002). Recent results from *Chandra* observations of W44 show that an elemental abundance gradient is present in this SNR, and that it has a significant contribution to the steepness of radial brightness profile (Shelton, Kuntz, & Petre 2004a). Accurate determination of elemental abundances and their distribution is therefore important in studying MM SNRs. HB 3 offers an interesting case because of the possibility of under-abundant Fe. Under-abundant Fe, in contrast to enhanced abundances of Ne, Si and S, have been found in W44. Shelton, Kuntz, & Petre (2004a) assign the Ne, Si and S enhancement to SN ejecta, and suggest that Fe originates from dust destruction and is under-abundant because Fe is still mostly condensed onto grains.

5. CONCLUSIONS

We present archival *ASCA* and *ROSAT* observations of three mixed-morphology SNRs, HB 21, CTB 1 and HB 3, as well as archival *Chandra* observations of CTB 1 and archival *XMM-Newton* observations of HB 3. As found in many other MM SNRs, the morphology of the SNRs is characterized by bright central emission and faint, diffuse emission that extends up to the radio boundary. There is a good correspondence between the *ROSAT* and *ASCA* features. We confirm the thermal origin of the central plasma and detect enhanced abundances, which imply the

presence of SN ejecta in these SNRs. HB 21 was found to have a single-component plasma temperature of ~ 0.6 keV and enhanced abundances of Si and S. *ASCA* and *Chandra* data of CTB 1 require a two-temperature thermal component, with a cooler component with $kT \sim 0.2$ keV having solar abundances, and warmer component with $kT \sim 0.8$ keV having enhanced abundances of Mg. *ASCA* data from HB 3 require a ~ 0.2 keV thermal component with enhanced abundances of Mg. *XMM* data from HB 3, however, allow for two possibilities — enhanced abundances of O and Mg, with column density and plasma temperature consistent with *ASCA* results, or different column density and plasma temperature values with either enhanced abundance of Ne or under-abundant Fe and solar O. We revise the list of SNRs suggested to be of MM type, and briefly examine some of their properties. A significant number of MM SNRs have been found to have enhanced abundances, which *Chandra* data of W44 have shown to be crucial for producing the steep radial brightness profile in MM SNRs (Shelton, Kuntz, & Petre 2004a).

ASCA observations revealed a compact source in the southern part of HB 3. The column density value found towards the source differs from that found towards the SNR and they are likely unrelated. The spectrum is best described with a power law model with photon index of ~ 2.7 , or a blackbody model with temperature of ~ 2 keV. The unabsorbed X-ray flux in the 0.5–10.0 keV band is $\sim 10^{-12}$ ergs cm $^{-2}$ s $^{-1}$.

We thank Manami Sasaki for help with *ROSAT* data reduction and Randall Smith for helpful comments. This research has made use of data obtained through the High Energy Astrophysics Science Archive Research Center Online Service, provided by the NASA/Goddard Space Flight Center. We acknowledge the use of NASA's SkyView facility (<http://skyview.gsfc.nasa.gov>) located at NASA Goddard Space Flight Center. This work was supported in part by the National Aeronautics and Space Administration through contract NAS8-39073.

REFERENCES

Angerhofer, P. E., Kundu, M. R., & Becker, R. H. 1977, *A&A*, 55, 11

Bamba, A., Yokogawa, J., Sakano, M., & Koyama, K. 2000, *PASJ*, 52, 259

Bocchino, F. & Bandiera, R. 2003, *A&A*, 398, 195

Borkowski, K. J., Lyerly, W. J., & Reynolds, S. P. 2001, *ApJ*, 548, 820

Brickhouse, N. S., Dupree, A. K., Edgar, R. J., Liedahl, D. A., Drake, S. A., White, N. E., & Singh, K. P. 2000, *ApJ*, 530, 387

Chakrabarty, D., Pivovaroff, M. J., Hernquist, L. E., Heyl, J. S., & Narayan, R. 2001, *ApJ*, 548, 800

Chen, Y., Su, Y., Slane, P. O., & Wang, Q. D. 2004, *ApJ*, 616, 885

Chevalier, R. A. 1999, *ApJ*, 511, 798

Cioffi, D. F., McKee, C. F., & Bertschinger, E. 1988, *ApJ*, 334, 252

Claussen, M. J., Frail, D. A., Goss, W. M., & Gaume, R. A. 1997, *ApJ*, 489, 143

Cox, D. P., Shelton, R. L., Maciejewski, W., Smith, R. K., Plewa, T., Pawl, A., & Różyczka, M. 1999, *ApJ*, 524, 179

Craig, W. W., Hailey, C. J., & Pisarski, R. L. 1997, *ApJ*, 488, 307

Dotani, T., Yamashita, A., Ezuka, H., Takahashi, K., Crew, G., Mukai, K., & the SIS Team, 1997, *ASCA News*, 5, 14

Enoguchi, H., Tsunemi, H., Miyata, E., & Yoshita, K. 2002, *PASJ*, 54, 229

Fesen, R. A., Downes, R. A., Wallace, D., & Normandeau, M. 1995, *AJ*, 110, 2876

Fesen, R. A., Winkler, F., Rathore, Y., Downes, R. A., & Wallace, D. 1997, *AJ*, 113, 767

Frail, D. A., Goss, W. M., & Slysh, V. I. 1994, *ApJ*, 424, L111

Frail, D. A., Goss, W. M., Reynoso, E. M., Giacani, E. B., Green, A. J., & Otrupcek, R. 1996, *AJ*, 111, 1651

Frail, D. A., & Mitchell, G. F. 1998, *ApJ*, 508, 690

Gaensler, B. M., Fogel, J. K. J., Slane, P. O., Miller, J. M., Wijnands, R., Eikenberry, S. S., & Lewin, W. H. G. 2003, *ApJ*, 594, L35

Green, A. J., Frail, D. A., Goss, W. M., & Otrupcek, R. 1997, *AJ*, 114, 2058

Green, D. A., & Dewdney, P. E. 1992, *MNRAS*, 254, 686

Guo, Z. & Burrows, D. N. 1997, *ApJ*, 480, L51

Hailey, C. J. & Craig, W. W. 1994, *ApJ*, 434, 635

Hailey, C. J. & Craig, W. W. 1995, *ApJ*, 455, L151

Harrus, I. M., Hughes, J. P., Singh, K. P., Koyama, K., & Asaoka, I. 1997, *ApJ*, 488, 781

Harrus, I. M., Slane, P. O., Smith, R. K., & Hughes, J. P. 2001, *ApJ*, 552, 614

Hendrick, S. P., Borkowski, K. J., & Reynolds, S. P. 2003, *ApJ*, 593, 370

Huang, Y.-L., & Thaddeus, P. 1986, *ApJ*, 309, 804

Humphreys, R. M. 1978, *ApJS*, 38, 309

Hwang, Ü., Petre, R., & Hughes, J. P. 2000, *ApJ*, 532, 970

Jones, T. W., et al. 1998, *PASP*, 110, 125

Kaplan, D. L., Frail, D. A., Gaensler, B. M., Gotthelf, E. V., Kulkarni, S. R., Slane, P. O., & Nechita, A. 2004, *ApJS*, 153, 269

Kawasaki, M., Ozaki, M., Nagase, F., Inoue, H., & Petre, R. 2005, *ApJ*, 631, 935

Kawasaki, M. T., Ozaki, M., Nagase, F., Masai, K., Ishida, M., & Petre, R. 2002, *ApJ*, 572, 897

Koo, B., & Moon, D. 1997, *ApJ*, 485, 263

Koo, B., Rho, J., Reach, W. T., Jung, J., & Mangum, J. G. 2001, *ApJ*, 552, 175

Koo, B., Lee, J., & Seward, F. D. 2002, *AJ*, 123, 1629

Koralesky, B., Frail, D. A., Goss, W. M., Claussen, M. J., & Green, A. J. 1998, *AJ*, 116, 1323

Landecker, T. L., Roger, R. S., & Dewdney, P. E. 1982, *AJ*, 87, 1379

Landecker, T. L., Dewdney, P. E., Vaneldik, J. F., & Routledge, D. 1987, *AJ*, 94, 111

Lazendic, J. S., Wardle, M., Burton, M. G., Yusef-Zadeh, F., Whiteoak, J. B., Green, A. J., & Ashley, M. C. B. 2002, *MNRAS*, 331, 537

Lazendic, J. S., Wardle, M., Burton, M. G., Yusef-Zadeh, F., Green, A. J., & Whiteoak, J. B. 2004, *MNRAS*, 354, 393

Leahy, D. A., Venkatesan, D., Long, K. S., & Naranan, S. 1985, *ApJ*, 294, 183

Leahy, D. A. 1987, *MNRAS*, 228, 907

Leahy, D. A. & Aschenbach, B. 1995, *A&A*, 293, 853

Leahy, D. A. & Aschenbach, B. 1996, *A&A*, 315, 260

Lockett, P., Gauthier, E. & Elitzur, M. 1999, *ApJ*, 511, 235

Lorimer, D. R., Lyne, A. G., & Camilo, F. 1998, *A&A*, 331, 1002

Lumb, D. H., Warwick, R. S., Page, M., & De Luca, A. 2002, *A&A*, 389, 93

Maeda, Y., et al. 2002, *ApJ*, 570, 671

Masai, K. 1997, *A&A*, 324, 410

Mavromatakis, F., Aschenbach, B., Boumis, P., & Papamastorakis, J. 2004, *A&A*, 415, 1051

Mazzotta, P., Mazzitelli, G., Colafrancesco, S., & Vittorio, N. 1998, *A&AS*, 133, 403

Morrison, R. & McCammon, D. 1983, *ApJ*, 270, 119

Pavlov, G. G., Sanwal, D., Garmire, G. P., & Zavlin, V. E. 2002, *ASP Conf. Ser.* 271: *Neutron Stars in Supernova Remnants*, eds. P. O. Slane & B. M. Gaensler, 247

Pavlov, G. G. 2003, *IAU Symposium No. 218*

Petruk, O. 2001, *A&A*, 371, 267

Pfeffermann, E. & Briel, U. G. 1986, *Proc. SPIE*, 597, 208

Raymond, J. C. & Smith, B. W. 1977, *ApJS*, 35, 419

Reach, W. T., & Rho, J. 1999, *ApJ*, 511, 836

Reach, W. T., Rho, J., & Jarrett, T. H. 2005, *ApJ*, 618, 297

Reich, W., Zhang, X., & Fürst, E. 2003, *A&A*, 408, 961

Rho, J.-H. & Petre, R. 1996, *ApJ*, 467, 698

Rho, J. & Petre, R. 1998, *ApJ*, 503, L167

Rho, J. & Borkowski, K. J. 2002, *ApJ*, 575, 201

Rho, J., Keohane, J. W., Pannuti, T. G., Borkowski, K., & Winkler, P. F. 2004, *AAS/High Energy Astrophysics Division*, No. 8

Routledge, D., Dewdney, P. E., Landecker, T. L., & Vaneldik, J. F. 1991, *A&A*, 247, 529

Safi-Harb, S., Dubner, G., Petre, R., Holt, S. S., & Durouchoux, P. 2005, *ApJ*, 618, 321

Sasaki, M., Plucinsky, P. P., Gaetz, T. J., Smith, R. K., Edgar, R. J., & Slane, P. O. 2004, *ApJ*, 617, 322

Sedov, L. I. 1959, *Similarity and Dimensional Methods in Mechanics*, New York: Academic Press, 1959

Seward, F. D. 1990, *ApJS*, 73, 781

Shelton, R. L., Cox, D. P., Maciejewski, W., Smith, R. K., Plewa, T., Pawl, A., & Różyczka, M. 1999, *ApJ*, 524, 192

Shelton, R. L., Kuntz, K. D., & Petre, R. 2004a, *ApJ*, 611, 906

Shelton, R. L., Kuntz, K. D., & Petre, R. 2004b, *ApJ*, 615, 275

Slane, P., Seward, F. D., Bandiera, R., Torii, K., & Tsunemi, H. 1997, *ApJ*, 485, 221

Slane, P., Smith, R. K., Hughes, J. P., & Petre, R. 2002, *ApJ*, 564, 284

Snowden, S. L., McCammon, D., Burrows, D. N., & Mendenhall, J. A. 1994, *ApJ*, 424, 714

Spitzer, L. 1956, *Physics of Fully Ionized Gases*, New York: Interscience Publishers

Sun, M., Seward, F. D., Smith, R. K., & Slane, P. O. 2004, *ApJ*, 605, 742

Tanaka, Y., Inoue, H., & Holt, S. S. 1994, *PASJ*, 46, L37

Tatematsu, K., Fukui, Y., Landecker, T. L., & Roger, R. S. 1990, *A&A*, 237, 189

Trümper, J. 1983, *Adv. Space Res.*, 2(4), 241

van den Bergh, S. 1978, *ApJS*, 38, 119

van Dishoeck, E. F., Jansen, D. J., & Phillips, T. G. 1993, *A&A*, 279, 541

Wardle, M. & Yusef-Zadeh, F. 2002, *Science*, 296, 2350

White, R. L. & Long, K. S. 1991, *ApJ*, 373, 543

White, N. E., Giommi, P., & Angelini, L. 2000, *VizieR Online Data Catalog*, 9031, 0

Willis, A. G. 1973, *A&A*, 26, 237

Yamamoto, F., Hasegawa, T., Morino, J., Handa, T., Sawada, T., & Dame, T. M. 1999, *Star Formation 1999*, Editor: T. Nakamoto, p. 110

Yamauchi, S., Koyama, K., Tomida, H., Yokogawa, J., & Tamura, K. 1999, *PASJ*, 51, 13

Yar-Uyaniker, A., Uyaniker, B., & Kothes, R. 2004, *ApJ*, 616, 247

Yoshita, K., Tsunemi, H., Miyata, E., & Mori, K. 2001, *PASJ*, 53, 93

Yusef-Zadeh, F., Roberts, D. A., Goss, W. M., Frail, D. A., & Green, A. J. 1996, *ApJ*, 466, L25

Yusef-Zadeh, F., Goss, W. M., Roberts, D. A., Robinson, B., & Frail, D. A. 1999, *ApJ*, 527, 172

Zimmermann, H. U., Becker, W., Belloni, T., et al. 1994, *EXSAS User's Guide* (MPE report 257)

TABLE 1
ARCHIVAL *ASCA* DATA USED IN THIS STUDY.

Source	Sequence number	Observing date	GIS exposure	SIS exposure	SIS mode
HB 21-P1	55053000	1997-06-09	39 ks	35 ks	1-CCD, bright
HB 21-P2	55054000	1997-06-10	38 ks	34 ks	1-CCD, bright
CTB 1-W	54026000	1996-01-21	58 ks	36 ks	2-CCD, bright
CTB 1-NE	54027000	1996-01-22	42 ks	37 ks	2-CCD, bright
HB 3-N1	54009000	1996-08-27	13 ks	12 ks	2-CCD, bright
HB 3-N2	54009010	1996-08-28	30 ks	23 ks	2×2 -CCD ^a , bright
HB 3-N3	54009020	1996-08-29	33 ks	29 ks	2-CCD, bright

^acomplementary mode

TABLE 2
ARCHIVAL *ROSAT* DATA USED IN THIS STUDY.

Source	Sequence number	Observing date	Exposure (s)
HB 21 - CENTER	500220n00	1998-07-23	4891
HB 21 - NE	500221n00	1998-07-23	2768
HB 21 - SE	500222n00	1998-07-23	3778
HB 21 - SW	500223n00	1998-07-23	708
HB 21 - NW	500224n00	1998-07-23	4442
HB 21 - N	500225n00	1998-07-23	4370
CTB 1 - FIELD 1	500155n00	1997-01-15	6291
CTB 1 - FIELD 2	500156n00	1997-01-15	8940
HB 3 - CENTER	500181n00	1996-10-23	2195
HB 3 - N	500182n00	1996-10-23	3069
HB 3 - SE	500183n00	1996-10-23	3906
HB 3 - SW	500184n00	1996-10-23	2949

TABLE 3

RESULTS FROM SPECTRAL MODELS FITS TO *ASCA* DATA OF HB 21, WITH THE 90% CONFIDENCE RANGES. FOR COMPARISON, WE LIST χ^2_ν VALUES FOR THE SOLAR AND ENHANCED ABUNDANCES CASES, AS WELL AS THE STATISTICAL SIGNIFICANCE OF THE IMPROVED FIT.

Parameter	P1-SIS (2SIS+2GIS) VNEI	P1-whole (2GIS) VNEI	P2-SIS (2GIS+2SIS) VNEI	P2-whole (2GIS) VNEI
N_H ($\times 10^{21}$ cm $^{-2}$)	$3.1^{+0.3}_{-0.2}$	$2.0^{+0.5}_{-0.5}$	$4.0^{+0.4}_{-0.2}$	$3.0^{+0.5}_{-0.5}$
kT (keV)	$0.63^{+0.03}_{-0.02}$	$0.58^{+0.04}_{-0.03}$	$0.68^{+0.03}_{-0.02}$	$0.64^{+0.04}_{-0.02}$
Si	$1.4^{+0.2}_{-0.3}$	$2.0^{+0.4}_{-0.3}$	$1.8^{+0.3}_{-0.3}$	$1.7^{+0.3}_{-0.3}$
S	1.0 ^a	$4.2^{+2.1}_{-1.7}$	1.0	$2.8^{+1.3}_{-1.2}$ ^a
n_{et} (cm $^{-3}$ s)	3.7×10^{13} ($\geq 3.4 \times 10^{13}$)	4.8×10^{13} ($\geq 4.1 \times 10^{13}$)	2.3×10^{13} ($\geq 2.0 \times 10^{13}$)	1.6×10^{13} ($\geq 1.3 \times 10^{13}$)
EM (cm $^{-3}$)	1.2×10^{55}	8.8×10^{55}	1.1×10^{55}	3.3×10^{55}
χ^2_ν /dof (solar)	1.38/236	1.07/302	1.29/232	1.07/337
χ^2_ν /dof (abund)	1.36/235	0.97/300	1.21/231	1.01/335
improvement	2σ	$> 4\sigma$	$> 3\sigma$	$> 4\sigma$

^aThe elemental abundance has been fixed at solar value.

TABLE 4

RESULTS FROM SPECTRAL MODELS FITS TO *ASCA* DATA OF CTB 1, WITH THE 90% CONFIDENCE RANGES. FOR COMPARISON, WE LIST χ^2_ν VALUES FOR THE SOLAR AND ENHANCED ABUNDANCES CASE, AS WELL AS THE STATISTICAL SIGNIFICANCE OF THE IMPROVED FIT.

Parameter center	W-SIS (2GIS+2SIS) VRAY+VRAY	W-whole (2GIS) VRAY	NE-whole (2GIS) VRAY	center (4ACIS) VNEI+VNEI
N_H ($\times 10^{21}$ cm $^{-2}$)	$5.2^{+0.8}_{-2.0}$	$7.5^{+0.8}_{-0.7}$	$8.7^{+0.7}_{-0.5}$	$5.7^{+0.7}_{-0.5}$
kT_1 (keV)	$0.19^{+0.09}_{-0.03}$	$0.26^{+0.03}_{-0.03}$	$0.18^{+0.00}_{-0.01}$	$0.20^{+0.04}_{-0.01}$
Mg ₁	1.0 ^a	1.0	1.0	1.0
$n_e t_1$ (cm $^{-3}$ s)	CIE	CIE	CIE	8.9×10^{12} ($\geq 1.5 \times 10^{12}$)
EM ₁ (cm $^{-3}$)	9.9×10^{56}	4.6×10^{57}	2.8×10^{58}	2.0×10^{56}
kT_2	$0.82^{+0.09}_{-0.06}$	—	—	$0.86^{+0.03}_{-0.06}$
Mg ₂	$2.7^{+0.9}_{-0.5}$	1.0	1.0	$3.1^{+1.0}_{-0.4}$
$n_e t_2$ (cm $^{-3}$ s)	CIE	—	—	1.4×10^{13} ($\geq 1.1 \times 10^{12}$)
EM ₂	9.6×10^{55}	—	—	1.9×10^{55}
χ^2_ν /dof (solar)	1.38/203	1.15/248	1.14/210	0.87/469
χ^2_ν /dof (abund)	1.29/202	—	—	0.80/468
improvement	$> 3\sigma$	—	—	$> 5\sigma$

^aThe elemental abundance has been fixed at solar value.

TABLE 5

RESULTS FROM SPECTRAL MODELS FITS TO *ASCA* DATA OF HB 3, WITH THE 90% CONFIDENCE RANGES. FOR COMPARISON, WE LIST χ^2_ν VALUES FOR THE SOLAR AND ENHANCED ABUNDANCES CASE, AS WELL AS THE STATISTICAL SIGNIFICANCE OF THE IMPROVED FIT.

Parameter	N2-SIS0 (2GIS+SIS) VRAY	N2-SIS1 (2GIS+SIS) VRAY	N3-north (2GIS+2SIS) VRAY	N3-south (2GIS+2SIS) VRAY	XMM-center ^a (pn) VRAY
N_H ($\times 10^{21}$ cm $^{-2}$)	$8.6^{+0.3}_{-0.3}$	$8.8^{+0.4}_{-0.3}$	$7.0^{+1.8}_{-0.7}$	$6.5^{+1.0}_{-1.4}$	$9.2^{+0.5}_{-0.6}$
kT (keV)	$0.18^{+0.02}_{-0.01}$	$0.18^{+0.02}_{-0.01}$	$0.27^{+0.03}_{-0.05}$	$0.29^{+0.07}_{-0.04}$	$0.18^{+0.02}_{-0.03}$
O	1.0 ^b	1.0	1.0	1.0	$1.9^{+0.4}_{-0.4}$
Mg	$2.6^{+0.6}_{-0.5}$	$1.6^{+0.6}_{-0.3}$ ^c	1.0	1.0	$2.0^{+0.7}_{-0.6}$
EM (cm $^{-3}$)	1.1×10^{58}	1.4×10^{58}	5.5×10^{56}	3.9×10^{56}	5.5×10^{57}
χ^2_ν /dof (solar)	1.56/274	1.60/280	1.25/144	1.36/188	1.22/2066
χ^2_ν /dof (abund)	1.42/273	1.56/279	—	—	1.19/2064
improvement	$> 4\sigma$	$> 3\sigma$	—	—	$> 5\sigma$

^asee section §3.3.2 for additional comments

^bThe elemental abundance has been fixed at solar value.

^cfit was not improved by thawing this elemental abundance

TABLE 6

SNR PARAMETERS DERIVED FROM SPECTRAL ANALYSIS USING THE CENTRAL SNR REGIONS AND DIFFERENT SNR EVOLUTIONARY MODELS.

Parameter	HB 21 P2-SIS	CTB 1 W-whole	HB 3 N2-SIS0
R (arcmin)	40	15	40
R (pc)	9.6	14.0	26.4
d (kpc)	0.8	3.1	2.2
V (cm^{-3})	2×10^{57}	5×10^{57}	8×10^{58}
Sedov model (adiabatic stage) ^a			
n_H (cm^{-3})	0.07 ± 0.01	0.15 ± 0.04	0.32 ± 0.10
kT_s (keV)	0.53 ± 0.03	0.20 ± 0.02	0.14 ± 0.02
v_s (km s^{-1})	670 ± 33	410 ± 45	340 ± 37
t_{SNR} (yr)	5600 ± 280	13100 ± 1440	30000 ± 3300
E_{SNR} (erg)	$(1.3 \pm 0.3) \times 10^{49}$	$(3.4 \pm 1.2) \times 10^{49}$	$(3.4 \pm 1.5) \times 10^{50}$
M (M_\odot)	0.16 ± 0.04	31 ± 11	31 ± 14
Evaporating clouds ^b			
kT_s (keV)	0.57–0.73	0.21–0.27	0.14–0.18
v_s (km s^{-1})	700–790	420–480	350–400
t_{SNR} (yr)	5400–4800	13000–11500	30000–25000
E_{SNR} (erg)	$(3–8) \times 10^{50}$	$(8–20) \times 10^{49}$	$(7–20) \times 10^{50}$

^acalculated for best-fit values from Tables 3 to 5

^bcalculated for range: $K/q = 1.0 – 1.3$ (see §4.2.1)

TABLE 7

A LIST OF MM SNRs AND SOME OF THEIR PROPERTIES; THE FIRST PART OF THE TABLE LISTS THE SNRs STUDIED BY RHO & PETRE (1998), AND THE SECOND PART LISTS OTHER SNRs SUGGESTED TO BE OF MM TYPE.

SNR Name	Enhanced abundances ^a	Multiple components	Molecular material	OH(1720 MHz) masers ^b
G6.4-0.1 (W28)	N (ASCA) [1]	Y [1]	Y [2]	Y [3]
G31.9+0.0 (3C 391)	N (ACIS) [4]	N [4]	Y [5]	Y [6]
G33.6+0.1 (Kes 79)	N (ACIS) [7]	N [7]	Y [8]	N [6]
G34.7-0.4 (W44)	Y (ACIS) [9]	N [9]	Y [10]	Y [11]
G41.1-0.3 (3C 397)	Y (ACIS) [12]	Y [12]	?	N [13]
<i>G43.3-0.2 (W49B)^c</i>	<i>ejecta?</i> [14]	—	—	—
G49.2-0.7 (W51C)	N (ASCA) [15]	Y [15]	Y [16]	Y [13]
G53.6-2.2 (3C 400.2)	N (ASCA) [17]	N [17]	?	?
G82.2+5.3 (W63)	Y (ROSAT+ASCA) [18]	Y [18]	?	?
G89.0+4.7 (HB21)	Y (ASCA) [19]	N [19]	Y [20]	N [6]
G93.7-0.2 (CTB 104A)	N (ROSAT) [21]	N [21]	?	N [6]
G116.9+0.2 (CTB 1)	Y (ASCA, ACIS) [19]	Y [189]	?	N [6]
<i>G119.5+10.2 (CTA 1)^d</i>	<i>PWN</i> [22]	—	—	—
G132.7+1.3 (HB 3)	Y (ASCA, pn) [19]	N [19]	Y [23]	N [6]
G189.1+3.0 (IC 443)	N (ASCA) [24]	Y [24]	Y [25]	Y [11]
G290.1-0.8 (MSH 11-61A)	Y (ASCA) [26]	N [26]	?	N [6]
<i>G327.1-1.1^d</i>	<i>PWN</i> [27]	—	—	—
G327.4+0.4 (Kes 27)	N (ASCA) [28]	N [28]	?	N (ATCA) [13]
<hr/>				
Sgr A East (G0.0+0.0)	Y (ACIS) [29]	N [29]	?	Y [30]
G65.3+5.7	N (ROSAT) [31]	N [31]	?	?
G156.2+5.7	Y (ASCA) [32]	N [32]	?	?
G160.9+2.6 (HB9)	N (ROSAT) [33]	N [33]	?	N [6]
G166.0+4.3 (VRO 42.05.01)	N (ASCA) [34]	N [34]	?	N [6]
G272.2-3.2	N (ASCA) [35]	N [35]	?	?
G357.1-0.1 (Tornado)	N (ACIS) [36]	N [36]	Y [37]	Y [38]
G359.1-0.5	Y (ASCA) [39]	Y [39]	Y [40]	Y [38]

^aindicates at the sensitivity observed with telescope noted in parenthesis

^bnon-detection with a single-dish telescope, unless telescope given in parenthesis

^cthe central emission might be ejecta-dominated, so the SNR might not belong to the MM class

^dthe central emission subsequently found to be dominated by non-thermal emission, so the SNRs do not belong to the MM class anymore

References. — [1] Rho & Borkowski (2002); [2] Reach et al. (2005); [3] Frail et al. (1994); [4] Chen et al. (2004); [5] Reach & Rho (1999); [6] Frail et al. (1996); [7] Sun et al. (2004); [8] Green & Dewdney (1992); [9] Shelton, Kuntz, & Petre (2004a); [10] Frail & Mitchell (1998); [11] Claussen et al. (1997); [12] Safi-Harb et al. (2005); [13] Green et al. (1997); [14] Hwang, Petre, & Hughes (2000); [15] Koo, Lee, & Seward (2002); [16] Koo & Moon (1997); [17] Yoshita et al. (2001); [18] Mavromatakis et al. (2004); [19] this work; [20] Koo et al. (2001); [21] Rho & Petre (1998); [22] Slane et al. (1997); [23] Huang & Thaddeus (1986); [24] Kawasaki et al. (2002); [25] van Dishoeck et al. (1993); [26] Slane et al. (2002); [27] Bocchino & Bandiera (2003); [28] Enoguchi et al. (2002); [29] Maeda et al. (2002); [30] Yusef-Zadeh et al. (1996); [31] Shelton, Kuntz, & Petre (2004b); [32] Yamauchi et al. (1999); [33] Leahy & Aschenbach (1995); [34] Guo & Burrows (1997); [35] Harrus et al. (2001); [36] Gaensler et al. (2003); [37] Lazendic et al. (2004); [38] Yusef-Zadeh et al. (1999); [39] Bamba et al. (2000); [40] Lazendic et al. (2002);

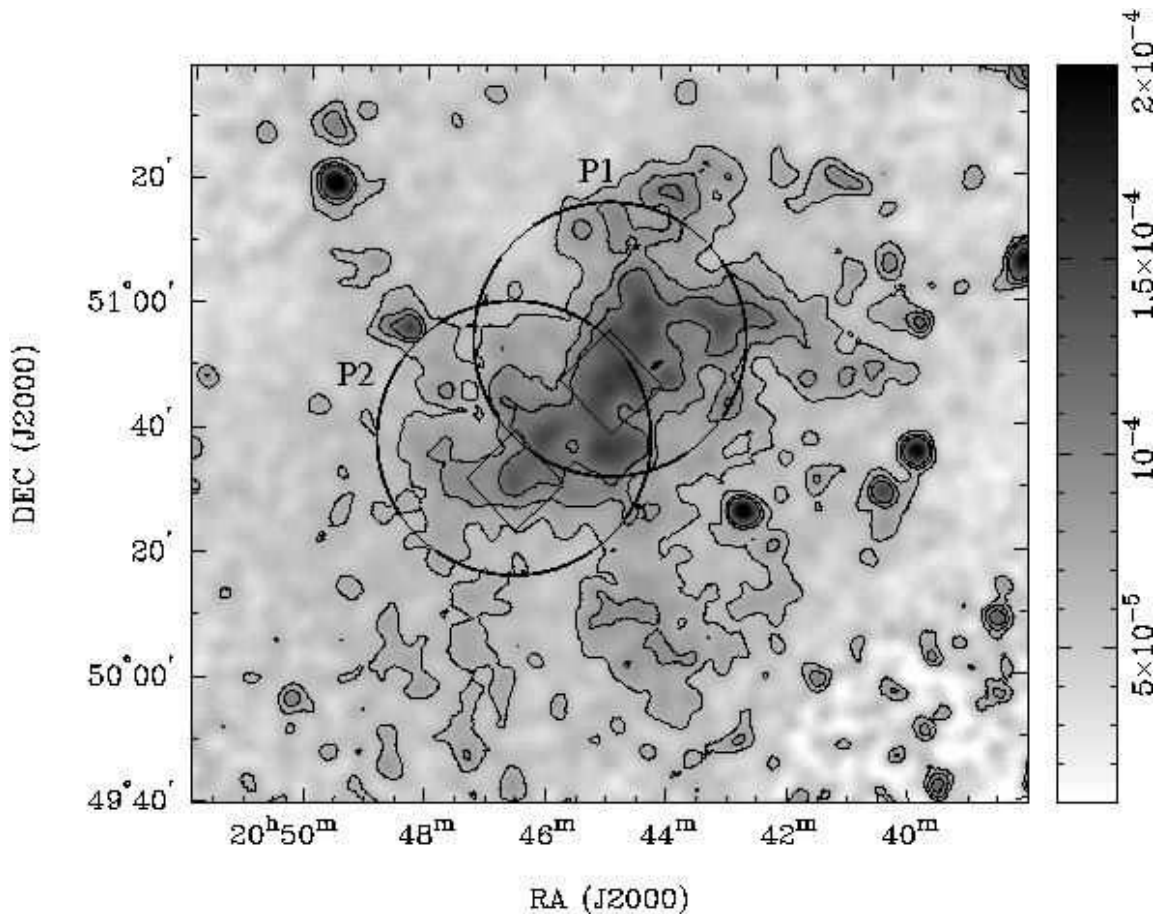


FIG. 1.— Exposure-corrected *ROSAT* PSPC greyscale and contour mosaic image of the SNR HB 21. The image has been smoothed with a 5'' FWHM Gaussian and units are in counts $\text{arcmin}^{-2} \text{ s}^{-1}$. The regions covered in two separate pointings (P1 and P2) with *ASCA* GIS detectors are marked with circles, and squares mark SIS detectors.

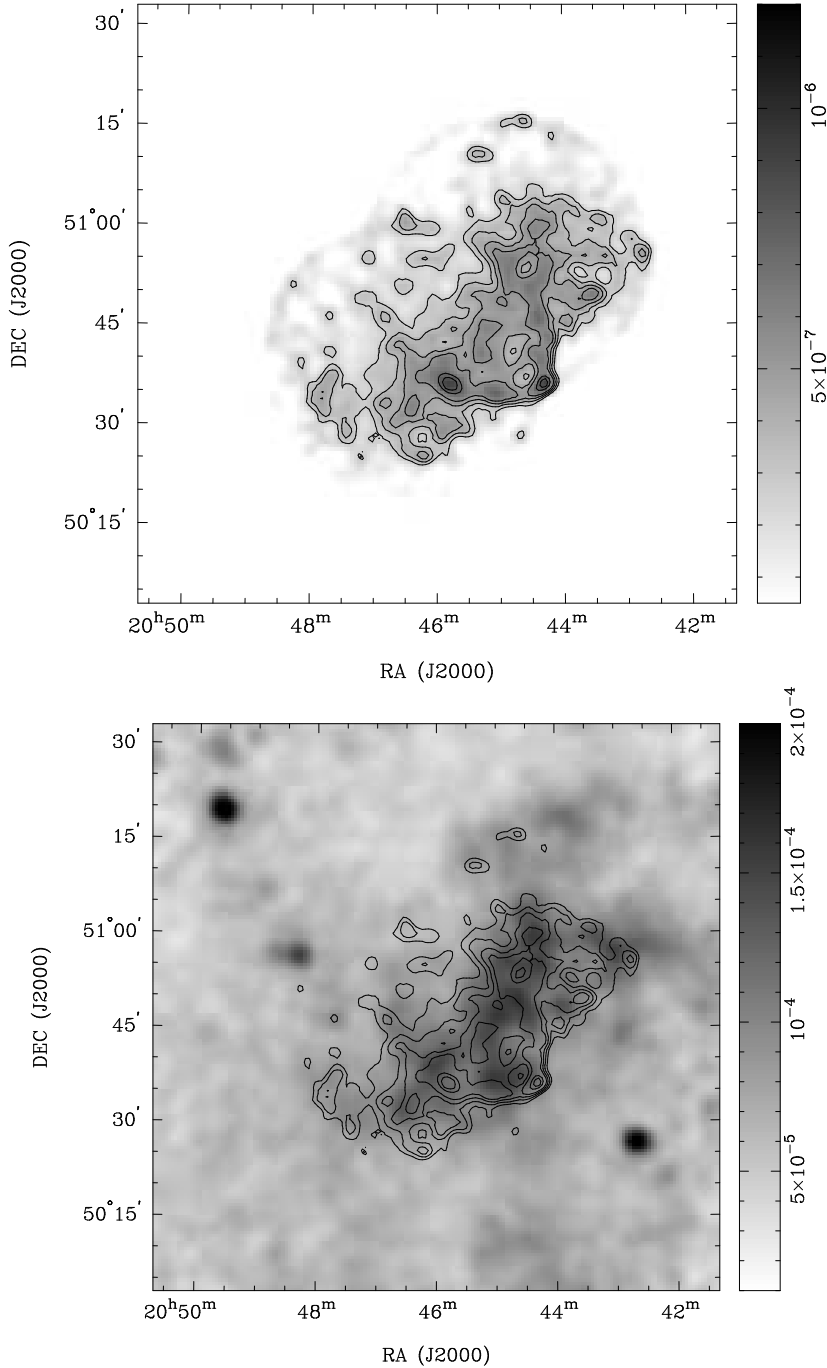


FIG. 2.— *Top*: Exposure-corrected and background *ASCA* GIS mosaic image of the central region of HB 21. The image has been smoothed with a $2''$ FWHM Gaussian and units are in counts $\text{arcmin}^{-2} \text{s}^{-1}$. *Bottom*: GIS contours overlaid onto the *ROSAT* greyscale image from Fig. 1. Contour levels are: $30, 40, 50, 60, 80, 90 \times 2 \times 10^{-8}$ counts $\text{arcmin}^{-2} \text{s}^{-1}$.

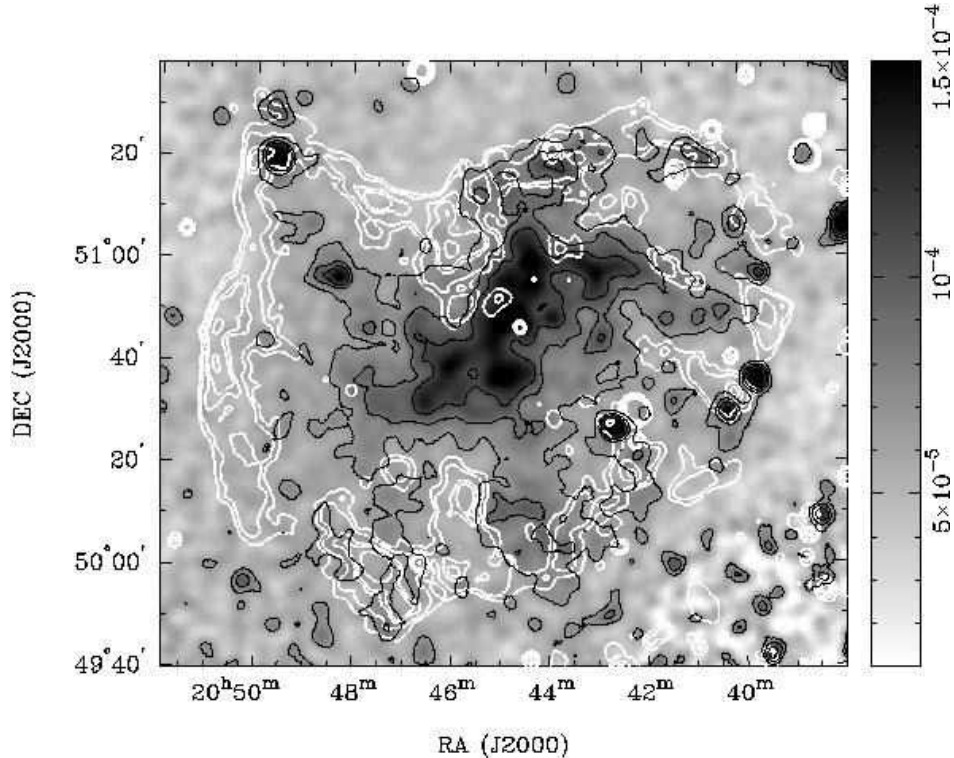


FIG. 3.— *ROSAT* PSPC image of HB 21 (greyscale and light black contours) overlaid with the 92 cm WENSS radio image (white contours), which has been smoothed to 2' resolution. Contour levels for the *ROSAT* image are same as in in Fig. 1, and radio (white) contours are: 4, 8, 16, 20, 30, 50, 70, 90 \times 0.01 Jy beam $^{-1}$. There is no radio emission corresponding the central X-ray emission. Faint diffuse emission is seen extending to the northern, southern and western SNR limb.

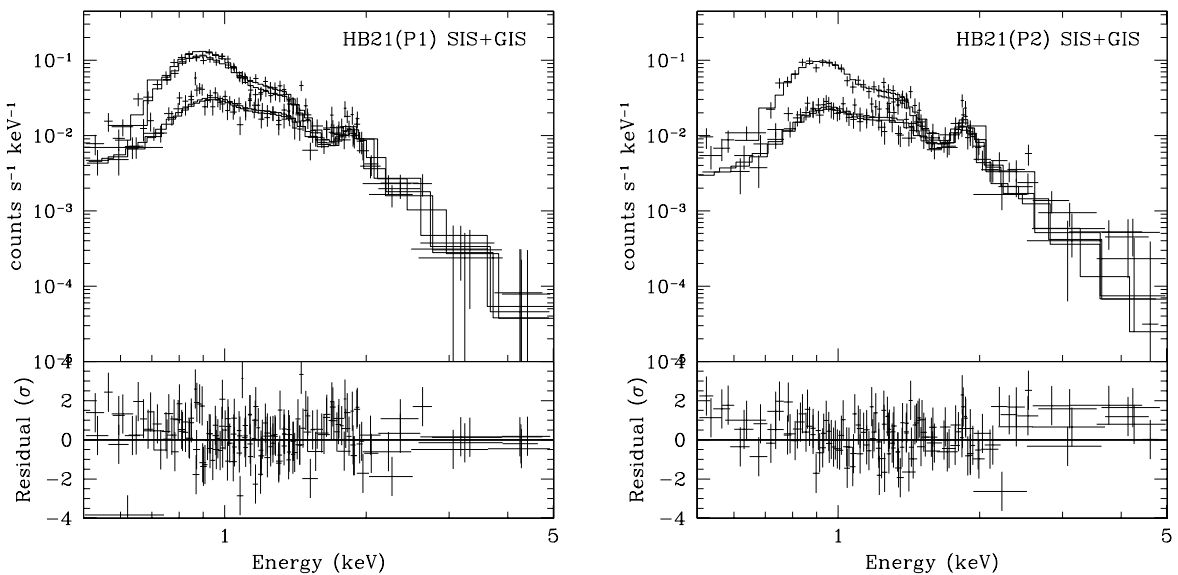


FIG. 4.— GIS and SIS spectra of the SNR HB 21 from the two *ASCA* pointings marked in Figure 1, common to GIS and SIS detectors, and residuals from the best-fit models. In all spectra the Si line is prominent. Fit parameters are listed in Table 3.

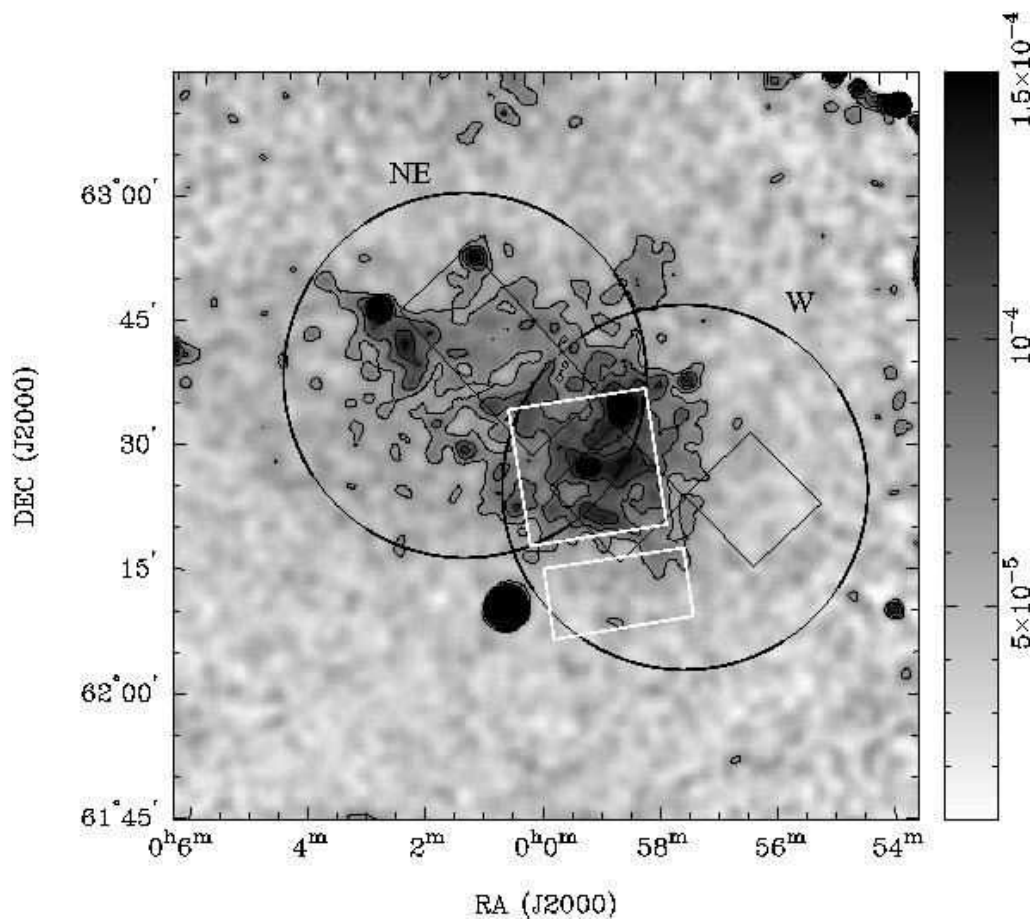


FIG. 5.— Exposure-corrected *ROSAT* PSPC greyscale and contour mosaic image of the SNR CTB 1. The image has been smoothed with a 3'' FWHM Gaussian and units are in counts $\text{arcmin}^{-2} \text{ s}^{-1}$. The regions covered in two separate pointings (NE and W) with the *ASCA* GIS detectors are marked with circles; black boxes mark the SIS detectors, and white boxes mark regions covered with the *Chandra* ACIS-I (white square) and ACIS-S (white rectangle) detectors.

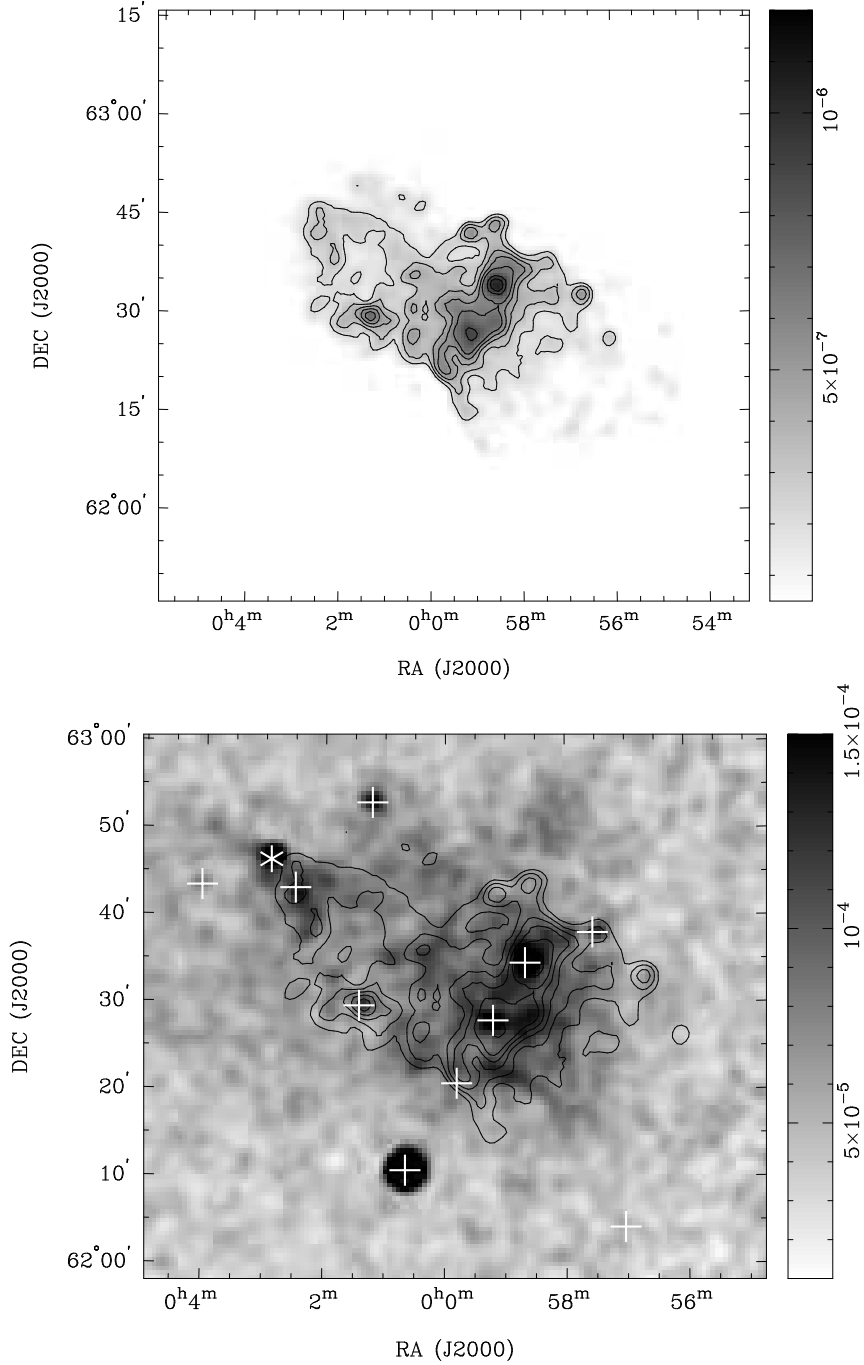


FIG. 6.— *Top:* Exposure-corrected and background-subtracted *ASCA* GIS mosaic image of CTB 1. The image has been smoothed with a $2''$ FWHM Gaussian and units are in counts $\text{arcmin}^{-2}\text{s}^{-1}$. *Bottom:* GIS contours overlaid on the *ROSAT* image from Fig. 5. Contour levels are: $20, 30, 40, 50, 60, 80, 90 \times 10^{-8}$ counts $\text{arcmin}^{-2} \text{s}^{-1}$. WGA point sources are marked with white crosses. The X-ray pulsar RXJ 0002+6246 (Hailey & Craig 1995), located north-east from the SNR, is marked with a star.

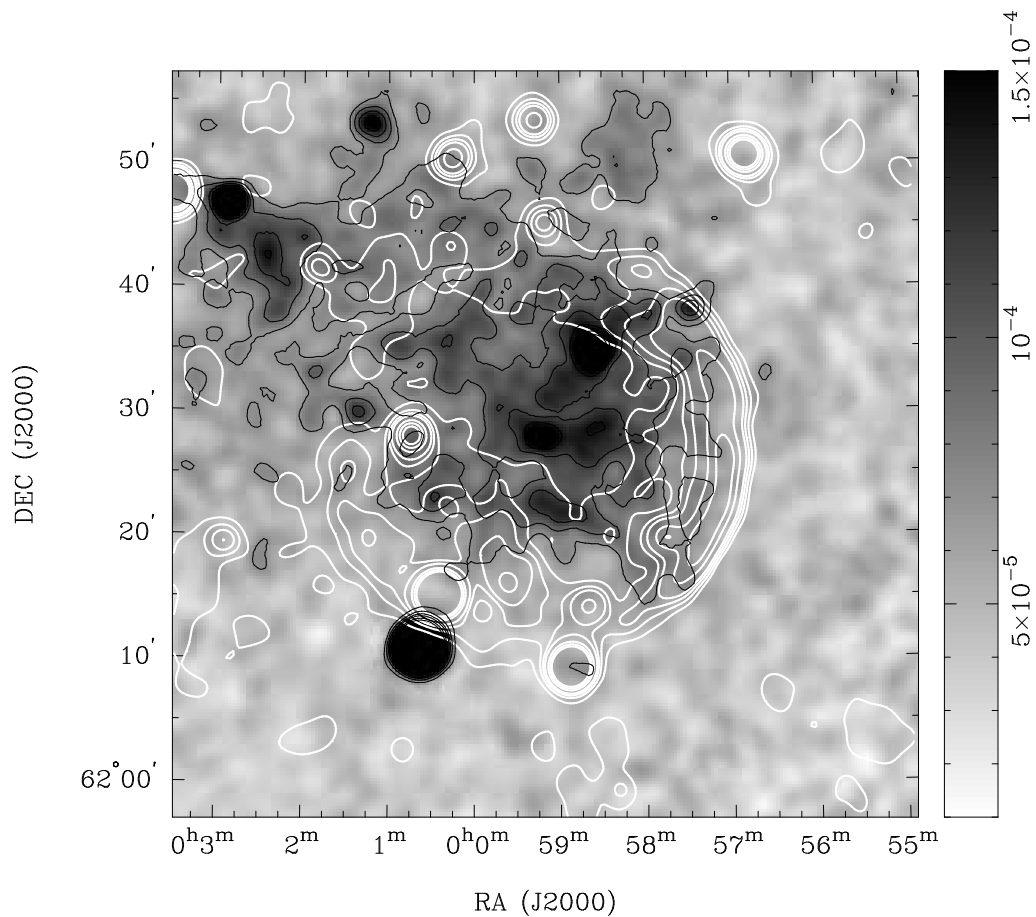


FIG. 7.—*ROSAT* PSPC greyscale image of CTB 1 overlaid with the 92 cm WENSS radio image, which has been smoothed to $2'$ resolution. Contour levels are: 1, 3, 5, 7, 12, 16, $20 \times 0.27 \text{ Jy beam}^{-1}$.

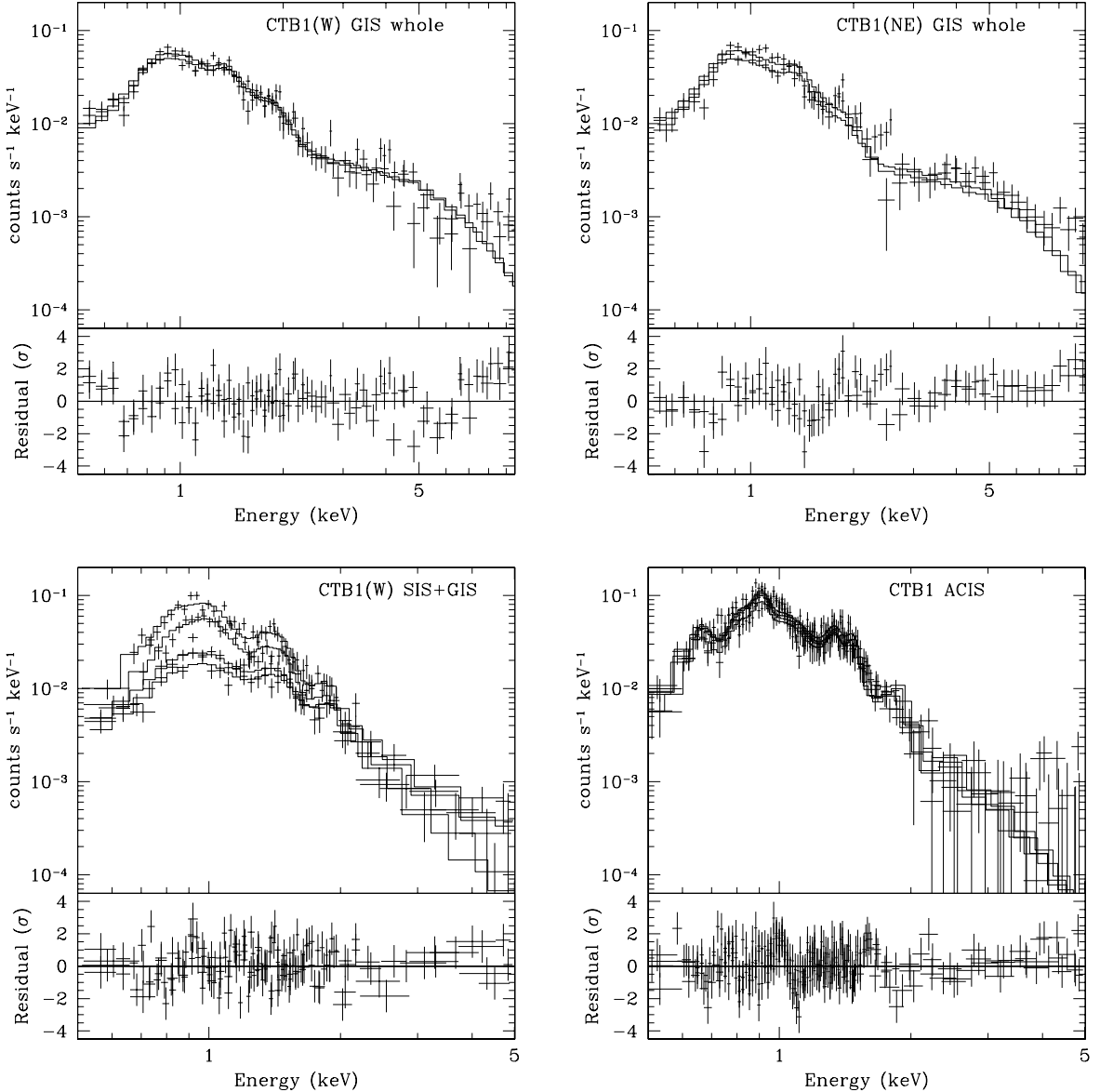


FIG. 8.— *ASCA* and *Chandra* spectra of the SNR CTB 1 and residuals from the best-fit models. The GIS and SIS spectra are from the two *ASCA* pointings marked in Figure 5, and the ACIS spectra are extracted from a 5' square regions located in the inner corner of each ACIS chip. Fit parameters are listed in Table 4. The Mg line is prominent in SIS+GIS spectra of the W *ASCA* region. In addition to Mg, O and Ne+Fe-L lines are visible in ACIS spectra.

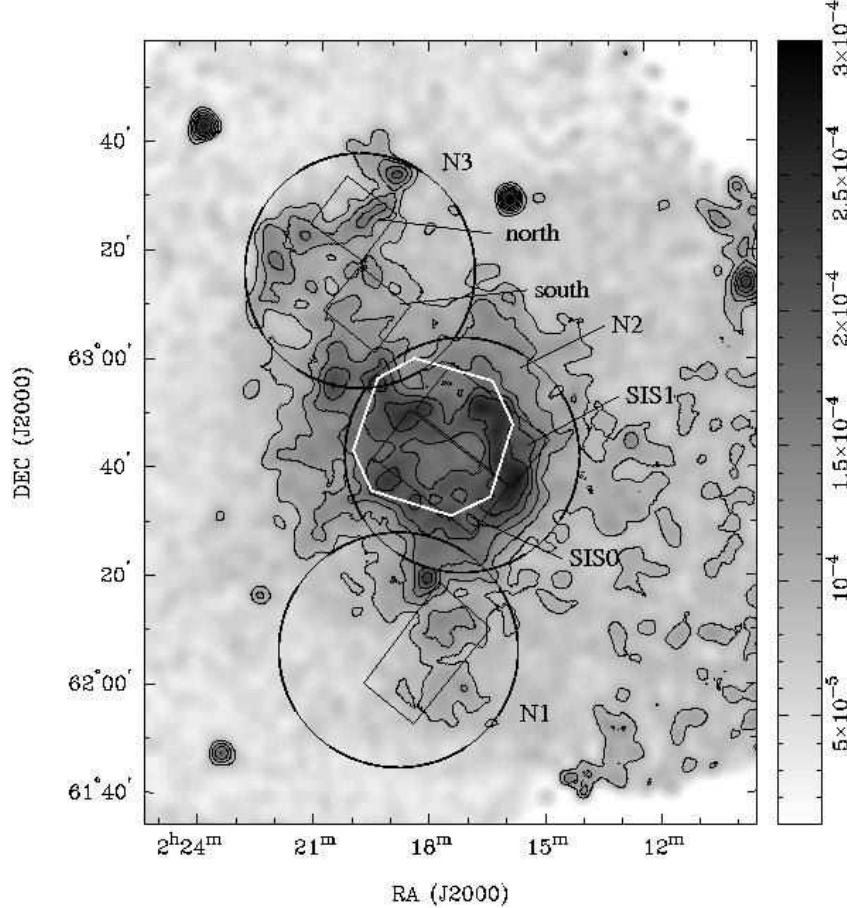


FIG. 9.— Exposure-corrected *ROSAT* PSPC greyscale and contour mosaic image of the SNR HB 3. The image has been smoothed with a 5'' FWHM Gaussian and units are in counts $\text{arcmin}^{-2} \text{ s}^{-1}$. The regions covered in three separate pointings (N1, N2 and N3) with *ASCA* GIS detectors are marked with circles, black boxes mark SIS detectors, and a white box marks region covered with *XMM-Newton* pn detector.

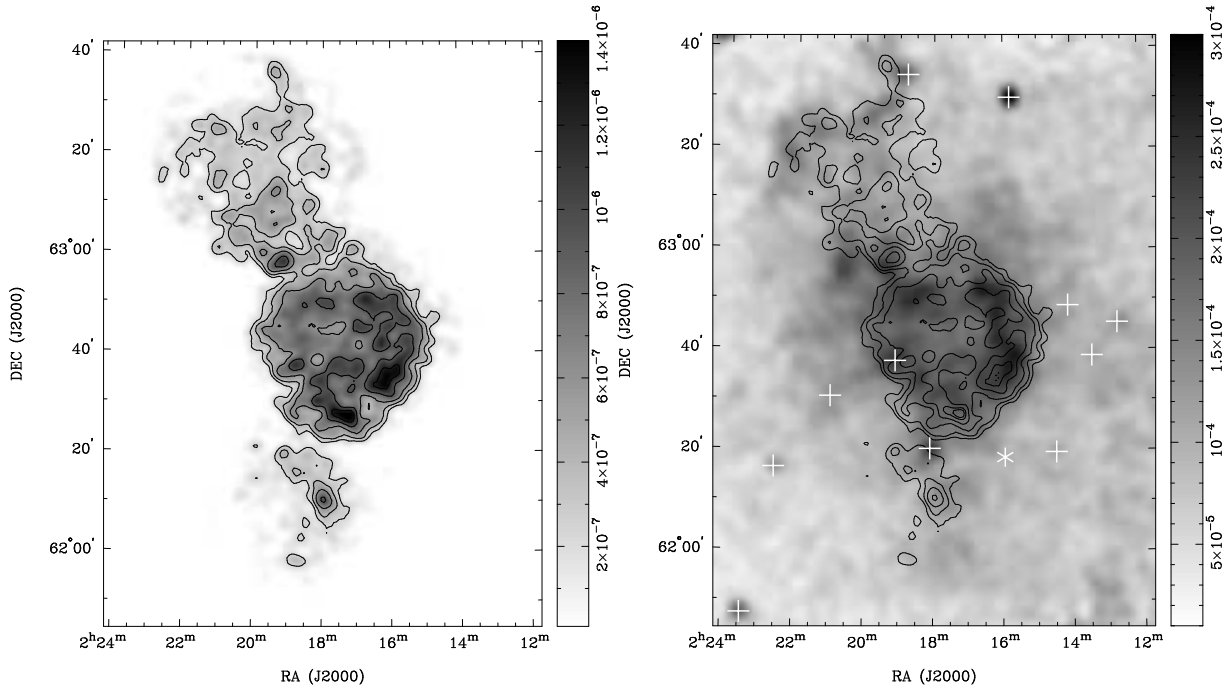


FIG. 10.— *Left*: Exposure-corrected and background-subtracted *ASCA* GIS mosaic image of three pointings towards HB 3. The image has been smoothed with a 2'' FWHM Gaussian and units are in counts $\text{arcmin}^{-2} \text{ s}^{-1}$. *Right*: GIS contours overlaid on the *ROSAT* image from Fig. 9. Contour levels are: 15, 25, 40, 50, 60, 80 $\times 1.5 \times 10^{-8}$ counts $\text{arcmin}^{-2} \text{ s}^{-1}$. The WGA point sources are marked with white crosses. The unrelated radio pulsar J0215+6218 (Lorimer, Lyne, & Camilo 1998), located in the south-western SNR region, is marked with a star.

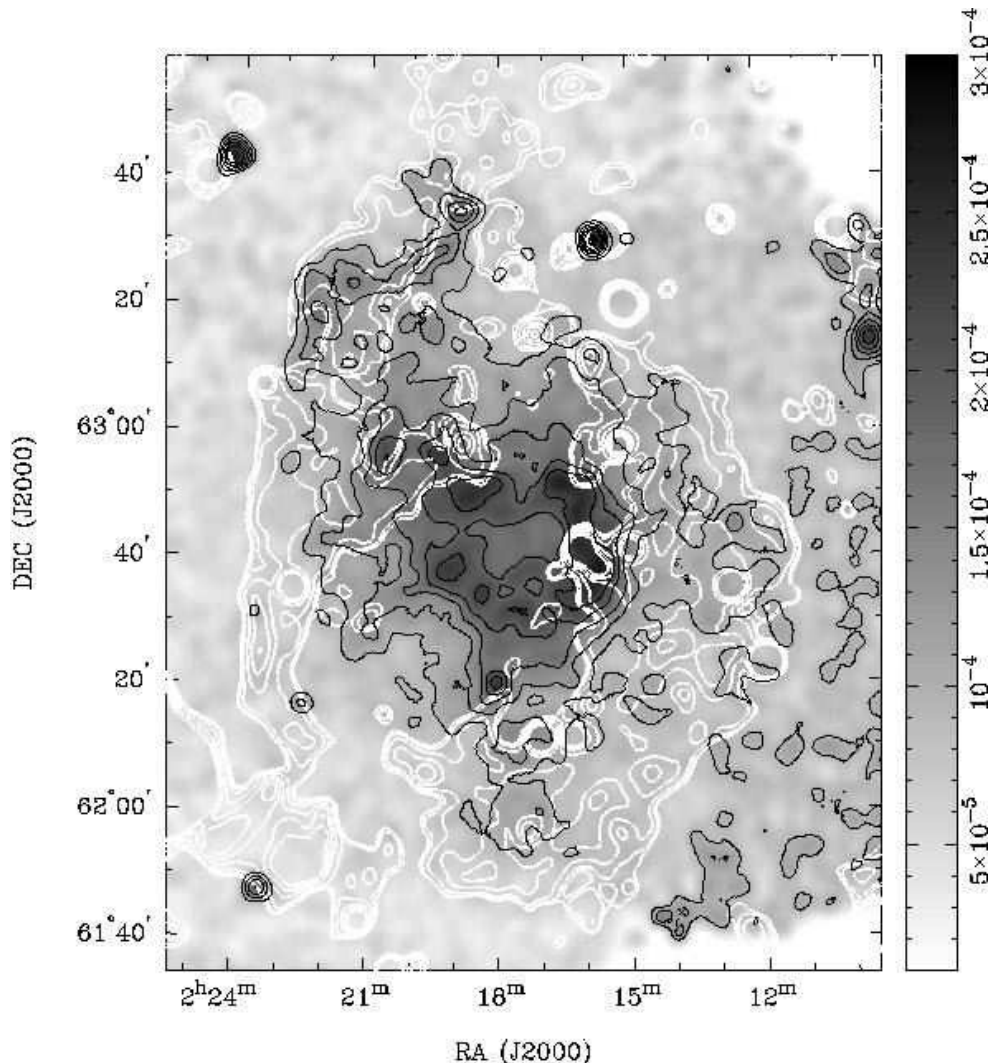


FIG. 11.— *ROSAT* PSPC greyscale image of HB 3 overlaid with the 92 cm WENSS radio image, which has been smoothed to $3'$ resolution. Contour levels are: $3, 10, 30, 50 \times 0.01 \text{ Jy beam}^{-1}$.

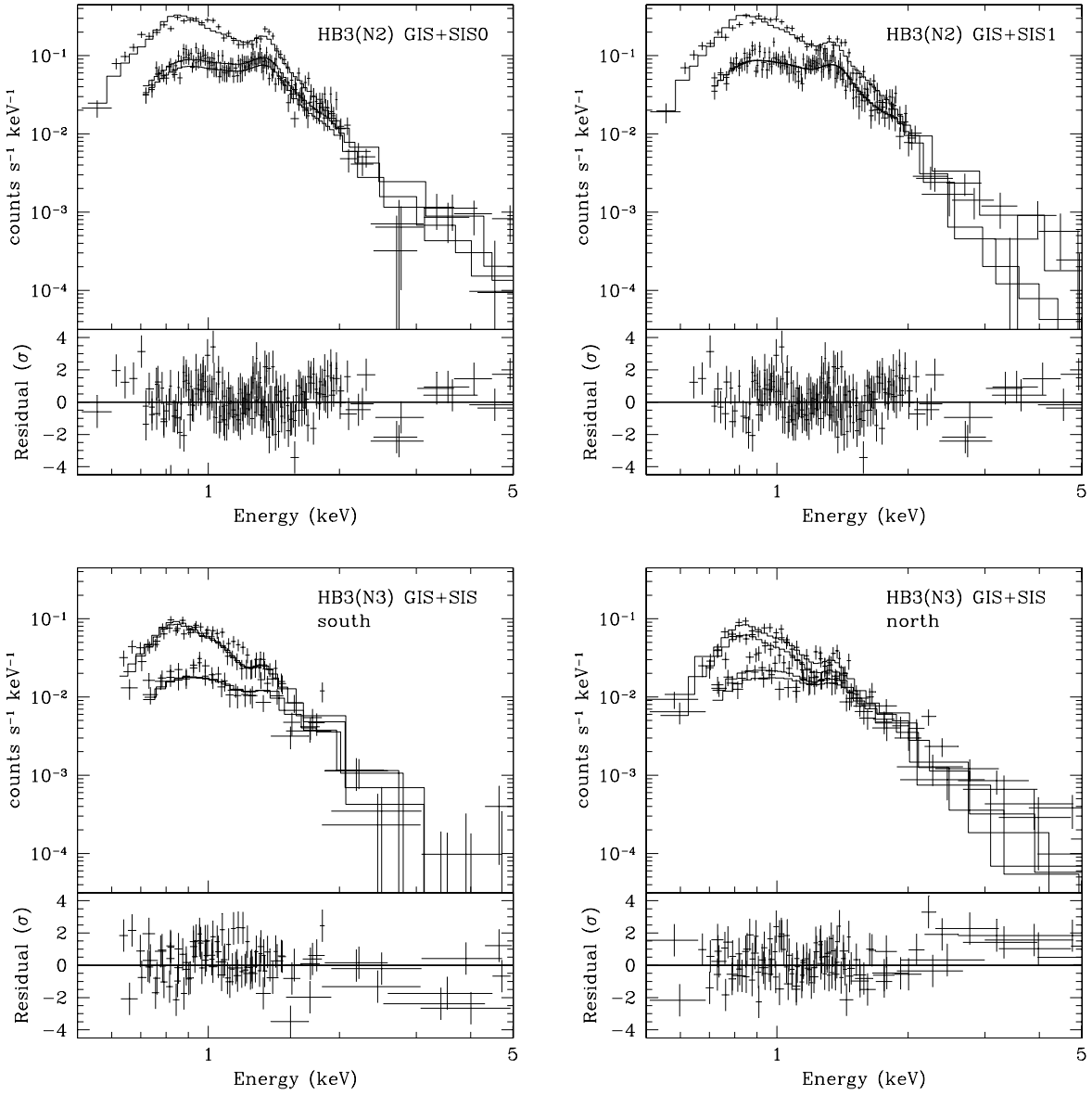


FIG. 12.— GIS and SIS spectra from the two *ASCA* pointings towards HB 3 marked in Figure 9, and residuals from the best-fit models. Fits parameters are listed in Table 5. Mg line is prominent in the spectra from N2 pointing.

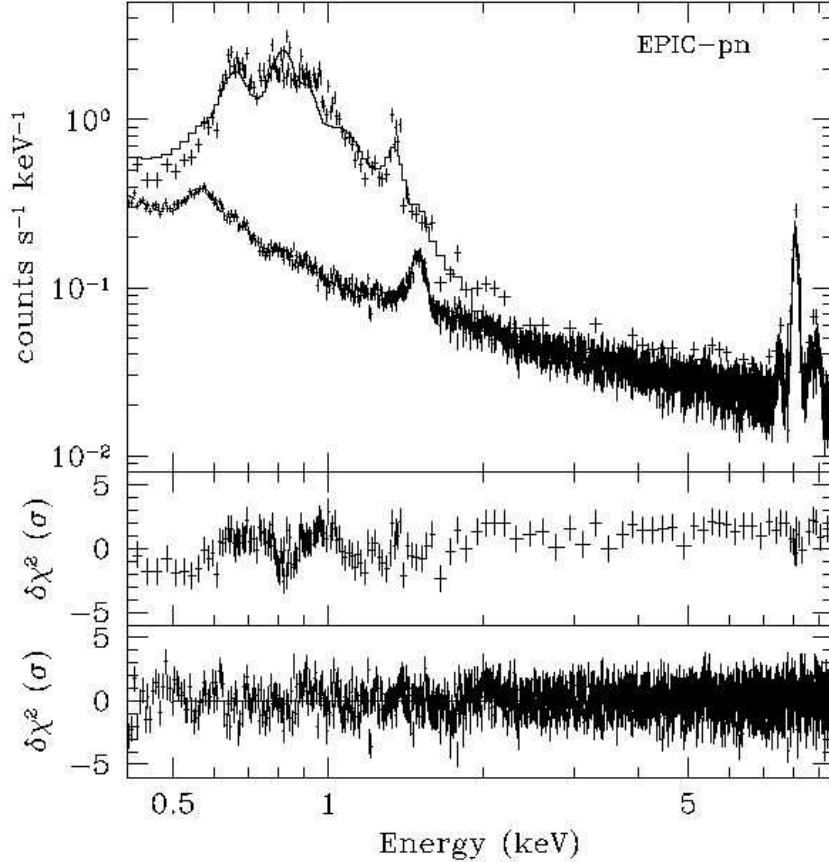


FIG. 13.— *XMM-Newton* EPIC-pn spectrum from the 5'-radius central region of HB 3. The spectrum of the source is fitted simultaneously with the background spectrum: the solid line in the upper panel represents source+background spectrum and its residuals from the best-fit model are given in the middle panel; the dashed line in the upper panel represents background spectrum and its residuals are given in the lower panel. The strong lines visible in the background spectrum are Al-K line at 1.5 keV and Cu-Ni-Zn-k line complex around 8 keV.

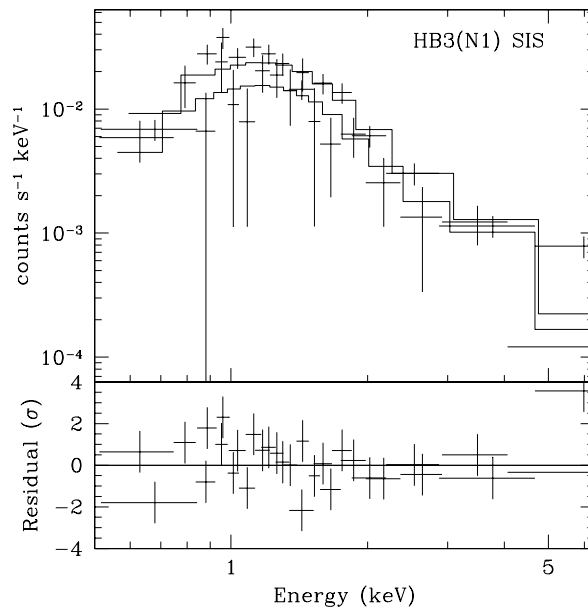


FIG. 14.— SIS spectra from the compact source located in the south N1 pointing towards HB 3, and residuals from the best-fit power law model. Fits parameters are listed in section § 3.3.3.

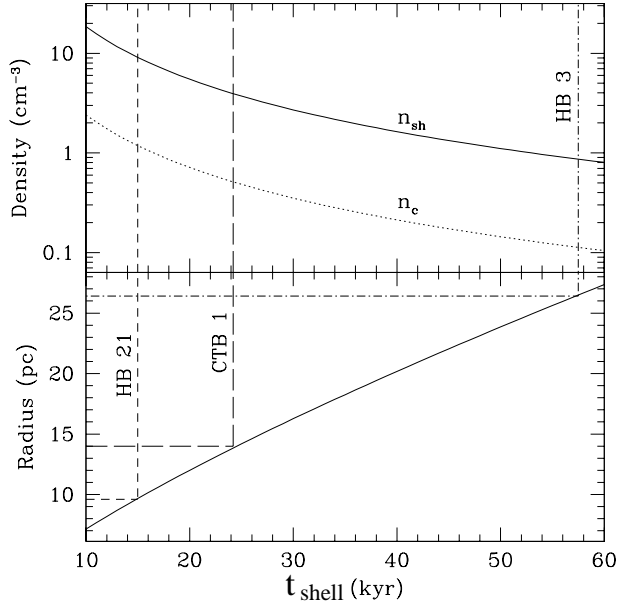


FIG. 15.—Properties of a supernova remnant at the time of radiative shell formation. The horizontal axis gives the age at which shell formation occurs, and the vertical axes give the corresponding radius (lower panel) and density (upper panel). The radii of HB 21, CTB 1, and HB 3, as determined from their radio shells, are indicated, along with corresponding values for the shell (n_{sh}) and central (n_c) densities. Note that uncertainties in the radius lead to uncertainties in the derived density and shell formation time, but these are not significant.